CSTAR Final Report

1 May 2016-30 April 2020

Collaborative Research on Improved Understanding and Prediction of Warm-Season (Derecho) and Cold-Season (Intense Mesoscale Snow Banding) High Impact Events

Principal Investigator: Robert Hart, Florida State University

Co-principal Investigator: Henry Fuelberg, Florida State University

Graduate Student: Derecho component: Vance Joyner (M.S., supervised by Fuelberg)

Graduate Student: Snowbanding component: Mark Nissenbaum (Ph.D., supervised by Hart)

Project Overview:

This project focuses on two types of high impact, low predictability mesoscale events: derechos and intense snowbanding.   For both foci of the project, the research goals are: 1) improved objective definition of the features, 2) creation of the most expansive database of the events, 3) development of an objective climatology of the database, 4) validation of existing tools for identifying or predicting the events, and 5) understanding the unique meteorology behind the various "flavors" (or sub-categories) of the two event types.

Summary of Research Accomplishments:

Derecho Accomplishments:

Previous progress reports described how our definition of a derecho was developed for use in this research. Specifically, we consulted the literature and our collaborators who have operational experience: Steve Weiss (Branch Chief, SPC), Steve Corfidi (Lead Forecaster, SPC), and Jeff Evans (MIC, HGX). The final definition was heavily motivated by Corfidi et al. (2015) to meet the operational objectives of the research. A derecho will be defined as a convectively induced, straight-line windstorm having the following characteristics:

1) A continuously progressing path of wind damage and/or severe wind gusts exceeding 25 m s^{-1}
(50 kt) that extends 650 km or greater along its major axis, and 100 km or greater along its minor axis,

2) No more than 2 h can pass between successive gust or damage reports,

3) Less than 200 km between gust or damage reports, and

4) Damage occurs after formation of a cold-pool mesoscale convective system that exhibits one or more sustained bow echoes with evidence of mesoscale vortices and/or rear inflow jets.

Both SPC storm reports and composite reflectivity were used to develop a list of derecho cases for the years 2006-2015 that meet the above criteria. The operational collaborators mentioned above assisted in classifying the more complex cases to ensure adherence to the definition. The final list of derecho cases can be found in Table 1.

Date	States Affected		Date	States Affected	
3-Jun-07	TX LA		20-Apr-11	AR KY IL IN	
18-Oct-07	KS MO		27-Apr-11	AL TN GA	
2-May-08	AR OK MO		11-Jul-11	IA IL IN MI	
1-Jun-08	AR AL MS		11-Jun-12	TN AR AL MS	
21-Jul-08	IA IL IN		29-Jun-12	OH IN IA VA WV MD	
31-Jul-08	MN WI IL		5-Aug-12	OH IN	
4-Aug-08	IL IA OH		13-Jun-13	OH IN PA	
3-May-09	TX LA MS		24-Jun-13	IA NE IL IN PA	
8-May-09	KS MO KY IL		5-Jun-14	AL GA	
12-Jun-09	AR MS AL		30-Jun-14	IL IN MO	2 derechos
16-Jun-09	KS MO KY		2-Oct-14	TX AR	
18-Jun-09	IA IL		22-Jun-15	SD MN IA WI IL	
18-Jun-10	IA IL IN OH		12-Jul-15	MN WI KY WV VA	
25-Feb-11	AL MS		18-Jul-15	MN WI	Test Case
4-Apr-11	TN AR MS KY AL GA		19-Jul-17	MN IA WI	

Table 1*: List of derecho cases from 2006-2017*

The Derecho Composite Parameter (DCP), as currently used by the SPC, is calculated using the following formula from Evans and Doswell (2001):

DCP = (DCAPE/980)(MUCAPE/2000)(0-6 km shear/20 kt)(0-6 km mean wind/16 kt)

We used a FORTRAN subroutine, modified from one originally written by George Bryan (UCAR), to calculate the DCAPE parameter for this formula.

As described in the previous progress report, plots of DCP and all of its components were generated for all cases. These plots showed that the NSSL-WRF model produced inconsistent and unrealistic DCP patterns that were not seen in plots from the GFS or HRW models. This unreliability is attributed to the WRF data archive only containing 7 vertical levels, introducing significant error in the calculation of MUCAPE and DCAPE because of their dependence on vertical integration. Based on this inconsistent

behavior, the use of the WRF for this research was discontinued in favor of focusing on the GFS because of its higher vertical resolution and greater temporal consistency.

To provide a quantitative approach to improving the DCP, binary regression was employed to find the parameters that are most distinctive to derecho formation. This required the selection of "null" cases for use in the regression, i.e., additional severe weather events that were not derechos. The null cases consisted of severe convective events that were not close to meeting either the temporal and/or spatial requirements for derecho classification.

Criteria for the null cases were developed to prevent them from being too similar to a derecho. Thus, a null case was defined as an organized multicell severe system that produced a swath of severe wind reports over 50 km in length, but no more than 420 km. The maximum length of 420 km was chosen since it is approximately 2/3 of the minimum length for derechos. The null cases were selected between longitudes 78W and 103W, so they occurred in the same region as a majority of the derechos that they are being compared against. The null case list consists of 27 events from 2006-2016 (Table 2). This number is similar to that of the derecho cases (Table 1).

24-May-06	5-Aug-08
22-Jun-06	19-Jun-09
19-Jul-06	19-Jun-10
21-Jul-06	2-Jul-10
10-Aug-06	28-Jun-13
11-Aug-06	11-Jun-14
19-Jun-07	15-Jun-16
16-Aug-07	17-Jun-16
27-Jun-08	

Table 2: *Dates of null cases from 2006-2016 to be used in binary regression.*

The initiation location of each null case had to be determined since they do not necessarily form a bow echo or LEWP as do derechos. Null initiation was defined to be the location of 55 dBZ composite reflectivity that occurs in the radar scan after the first storm report associated with the null storm report swath.

The environments in which derechos and null cases formed were quantitatively analyzed, Specifically, values of various parameters within a grid surrounding the initiation point of the null and derecho events were compiled to be used in the binary regression. The grid consisted of 9 points formed by the initiation point in the middle and the eight adjacent GFS gridpoints in all directions. This formed a 110 × 110 km square grid of values since the GFS has a horizontal resolution of 0.5°. The eighteen parameters listed below were considered in the regression that was done using MATLAB. The maximum

value within the 9-point grid for each parameter at the 0-hour forecast was used as the input for the regression.

- Surface CAPE, MUCAPE, DCAPE, Surface CIN
- Shear and the mean wind between 0-1 km, 0-3 km, 0-6 km, 0-10 km
- Downdraft temperature, difference between Downdraft Temperature and the Surface Temperature
- Lapse Rate between 0-3 km, 0-6 km, 3-7 km, and the vertical θ_e gradient between 1-5 km

The small size of the case list (31 derechos, 27 null) posed a problem for both creating and testing any formula from regression. Training and then testing the regression analysis on the full data set was not acceptable since that would only give information on how well these specific 58 cases could be predicted. Splitting the data so that half would be used as a training set, and the other half used to test the results would yield even smaller numbers of derecho and null cases. Their use almost certainly would have led to overfitting such that the regression equation would produce poor results on other cases.

To solve this issue, bootstrapping was used to artificially expand the available data. A different random sample of 45 cases was selected 500 times, and regression analysis with forward selection and backwards elimination was performed on each sample. The selection threshold was a p-value of 0.05, and the removal threshold p-value is 0.10.

It would be unrealistic to use every parameter that was selected in one of the 500 iterations of the bootstrapping method. Therefore, the four most often selected parameters out of all 500 samples were picked to create our new Derecho Prediction Parameter (DPP). These four, and their frequency of selection are:

1. Downdraft Temperature, 468
2. 0-6 km Shear, 315
3. 0-3 km Shear, 254
4. 0-6km Lapse Rate, 234

The next closest parameter in terms of frequency was 0-1 km shear, with 150 occurrences. Being selected less than one-third of the time seemed too infrequent to be used.

The median regression coefficient was determined for each of the above four parameters and then all coefficients were summed with a median intercept value from the regression analysis to create one combined parameter, the DPP. The resulting formula for the DPP is:

$$DPP = 0.11435 * Shear6 + 0.152865 * Shear3 + 0.34503 * DownT - 0.94398 * Lapse6 - 95.707$$

To analyze how values of the DPP differ between the null and derecho cases, a box and whisker plot was created when the DPP was applied to the 0-hr forecasts (Figure 1). There is a clear division between the top three quartiles for derecho cases (orange) and the bottom three quartiles of the null cases (blue) is evident, with the split occurring near DPP = 4.
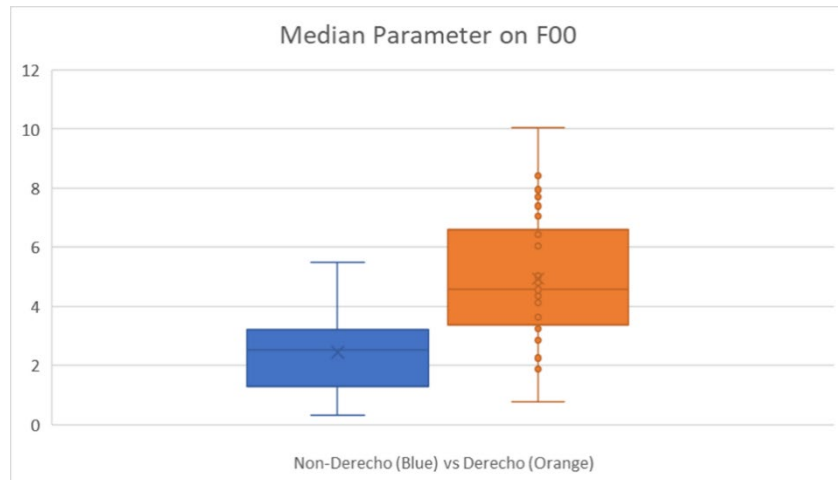

Figure 1: *Box and whisker plot comparing DPP values for the null and derecho cases. The key feature is the clear division between the two sets near the value of 4. This value is used as the basis for differentiating between what will be forecast as a derecho or non-derecho event out to 36 h.*

Using DPP = 4 as a threshold for predicting a derecho (greater than 4) vs a non derecho event (less than 4), the effectiveness of the new parameter was evaluated out to a 36 h forecast (Table 3). It is clear that the new DPP parameter gives very few false alarms regardless of lead time. The accuracy and reliability greatly increase when the lead time decreases to 12 h. This is expected since forecasts are inherently more accurate closer to an event. *We are excited about these favorable results.*

Forecast Hour	Total Correct of 58	False Alarm	Correct Null	Missed	Correct Derecho
0	44	4	23	10	21
12	43	3	24	12	19
24	36	2	25	20	11
36	36	3	24	19	12

Table 3: *Performance information of the DPP, including total correct, false alarms, and missed derechos.*

The next step is to compare the performance of the parameter developed here with the currently used Derecho Composite Parameter. We also will evaluate the individual parameters that comprise the DPP regarding how they differ in derecho and null events.

We present base reflectivity for an example derecho case (Figures 2, 3, 4) that initiated at approximately 0200 UTC 18 July 2015. The derecho traveled from the intersection of North Dakota, South Dakota, and Minnesota to southern Michigan.
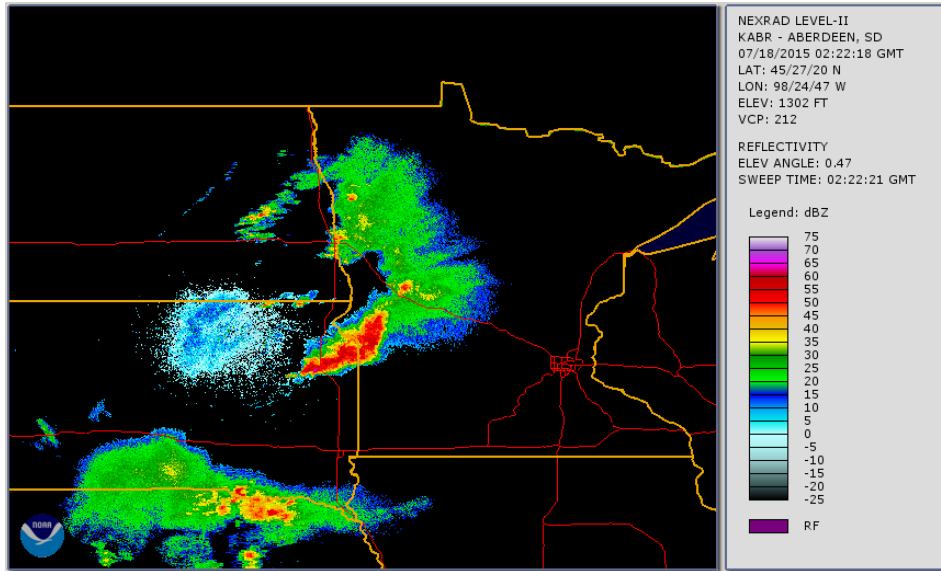

Figure 2: *Base reflectivity of the example case just after initiation on 0200 UTC 18 July 2015.*
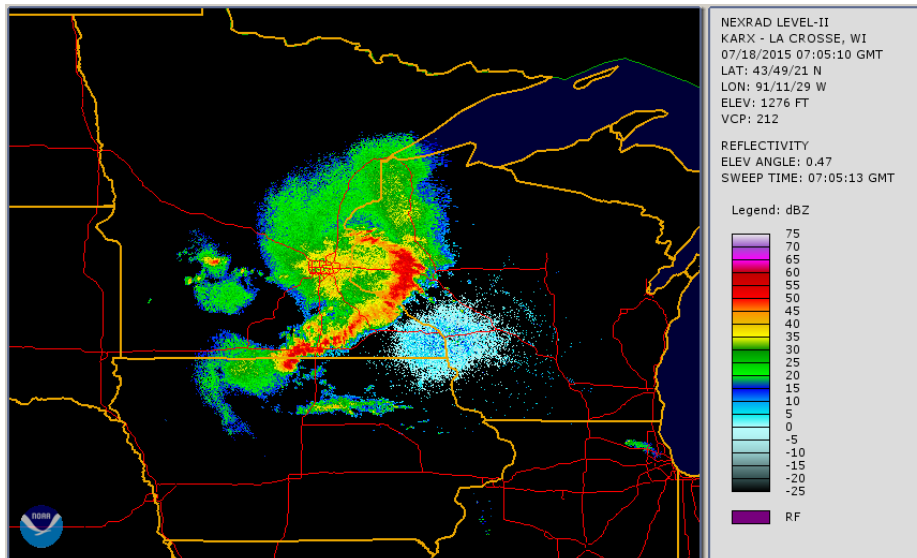
Figure 3: *Base reflectivity of the example case near peak strength as it enters Wisconsin near 0700 UTC on 18 July 2015. The bow echo structure is evident, as well as bookend vortices.*
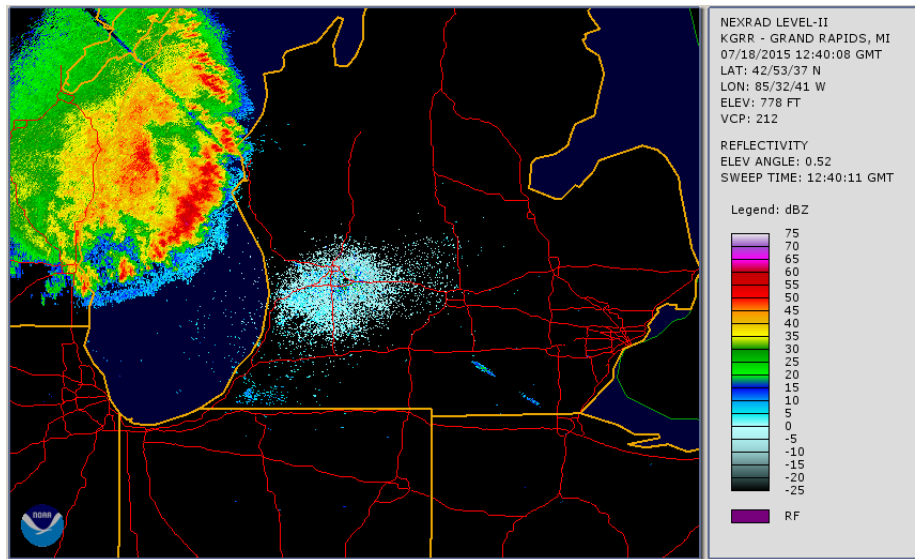
Figure 4: *Base reflectivity of the example case as it begins to weaken near 1300 UTC 18 July 2015. The bookend vortices are no longer pronounced.*

A comprehensive summary of the very promising results for all the cases in the derecho case list will be provided in the M.S. Thesis of Mr. Vance Joyner (supervised by Fuelberg).

Snowbanding Accomplishments:

Although modern numerical weather prediction (NWP) models contain sophisticated physics parameterizations with cloud-resolving grid scales, predictability barriers remain when forecasting snowfall from mesoscale snow bands, particularly in Northeast U.S. winter storms. In fact, due to the nature of mesoscale snow bands, a powerful midlatitude cyclone is not a necessary condition for heavy snowfall (Nicosia and Grumm 1999). And while it is well known what processes contribute to mesoscale snow band formation, there is interest in knowing if these features are resolved explicitly by the NWP models or if traditional proxy-based methods perform better at diagnosing areas favorable for banding.

Causes of Mesoscale Snow Bands

Role of Frontogenesis

During cyclogenesis, the horizontal thermal gradient tightens, and frontal features become prominent. As the thermal gradient increases, frontogenesis develops, and thermal wind balance is disrupted. Frontogenesis is of interest because the responding ageostrophic circulation creates ascent to restore thermal wind balance (Lackmann 2012). Frontogenesis has been present in a number of case studies involving mesoscale snow bands (e.g., Nicosia and Grumm 1999; Novak et al. 2004; Schultz and Knox 2007).

A simplified mathematical equation for frontogenesis was described by Miller (1948) under the assumption that changes to the thermal gradient are due to the flow pattern of air parcels along a Lagrangian reference frame. This equation is represented in geostrophic form by

$$F = \frac{1}{|\nabla\theta|}\left[-\frac{\partial\theta}{\partial x}\left(\frac{\partial u_g}{\partial x}\frac{\partial\theta}{\partial x} + \frac{\partial v_g}{\partial x}\frac{\partial\theta}{\partial y}\right) - \frac{\partial\theta}{\partial y}\left(\frac{\partial u_g}{\partial y}\frac{\partial\theta}{\partial x} + \frac{\partial v_g}{\partial y}\frac{\partial\theta}{\partial y}\right)\right],$$

where θ is the potential temperature. Essentially, frontogenesis is controlled by shearing/stretching along the front-parallel wind component and confluence/difluence of the horizontal wind acting on the gradient of potential temperature. An example of shearing strengthening the thermal gradient occurs when temperature advection increases normal to a cold front, enhancing frontogenesis. However, when advection increases normal to a warm front, easterly flow on the poleward side of the front decreases the thermal gradient, and frontolysis results. The confluent term can modify frontogenesis depending on the angle between the axis of dilation of the deformation zone and its orientation with the thermal gradient. When this angle is less than 45°, the thermal gradient increases, and frontogenesis is enhanced (Lackmann 2012; Nicosia and Grumm 1999).

Role of Equivalent Potential Vorticity (EPV)

For several decades now, slantwise convection has been explored as a potential contributor to the development of multiple snow bands within winter storms. A popular method for assessing the potential for slantwise convection is conditional symmetric instability (CSI). CSI assumes that an air parcel is stable to both inertial and gravitational forces, but unstable to perturbations along slantwise surfaces; an excellent example of this concept is shown in Figure 5. Slantwise convection is present in environments that are statically stable, otherwise vertical updrafts are preferred. The concept of CSI was famously critiqued by Schultz and Schumacher (1999) for being overused in the explanation of mesoscale snow bands as the conditions for moisty symmetric instability (MSI) depend heavily on the thermodynamic assumptions.

CSI occurs in baroclinic environments that feature large vertical wind shear, large scale rising motion, nonexistent or anticyclonic horizontal wind shear, near saturation (as saturation is a condition for CSI release), and near neutral stability to prohibit upright convection (Moore and Lambert 1993). On a cross section oriented perpendicular to the thermal wind vector, CSI is favored in regions where the saturated equivalent potential temperature (θ_{es}) surface is more steeply sloped than the M_g surface (Nicosia and Grumm 1999). This typically occurs under conditions with low static stability and large vertical wind shear.
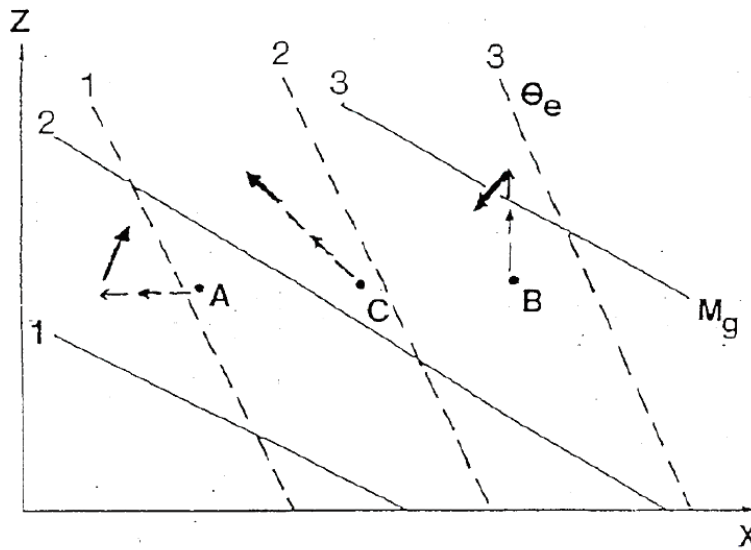
Figure 5: *Symmetric stability is visualized using air parcels traveling in several directions. Geostrophic momentum, M*g*, is drawn as the solid line and potential temperature is drawn as the dashed line. Parcel A is inertially stable to horizontal motions, so it will rise until it becomes gravitationally stable. Eventually parcel A will return to its original position. Similarly, parcel C is gravitationally stable, but will later become inertially stable and return to its initial position. However, when pushed along a sloped path, parcel C is both inertially and gravitationally unstable, so it will continue rising along the slantwise surface. From Bosart and Sanders (1986).*

On conventional radar imagery, CSI-induced rain or snow bands are oriented approximately parallel to the thermal wind vector with widths on the order of 50-100 km, lengths ranging from 100-400 km, and durations lasting up to 3-4 hours. Additionally, the bands may exist within stratiform precipitation shields and can coexist with frontal bands. The precipitation bands produced by CSI feature slanted updrafts and downdrafts (Figure 6). Although CSI is mostly a cold season phenomenon, it has been studied in the stratiform regions of mesoscale convective systems (MCSs) where anticyclonic shear is present on the poleward part of the system. Also, it is theorized that CSI may enhance the linear organization of convective lines even without the presence of CSI-type bands.

A commonly used diagnostic method to determine if the environment is predisposed to slantwise convection is the equivalent potential vorticity (EPV). It is computed mathematically as

$$\text{EPV} = g\left[\left(\frac{\partial M_g}{\partial p}\frac{\partial \theta_{es}}{\partial x}\right) - \left(\frac{\partial M_g}{\partial x}\frac{\partial \theta_{es}}{\partial p}\right)\right],$$
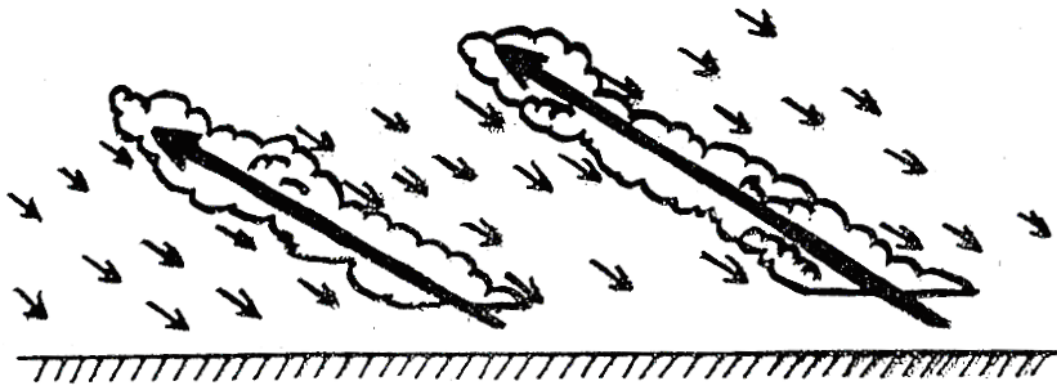
9

Figure 6: *Conceptual diagram of slantwise convective updrafts and downdrafts associated with CSI. The updrafts are thin and narrow compared to the broad downdrafts. From Klemp et al. (1984).*

with geostrophic momentum given by $M_g = V_g + fx$, where V_g is the geostrophic wind, f is the Coriolis parameter, θ_{es} is the saturation potential temperature, and x is the distance orthogonal to the thermal wind vector. There is debate at large regarding the usage of geostrophic versus the full wind when calculating EPV (Schultz and Schumacher 1999). Novak et al. (2004) argue that usage of the full wind is more representative of the curved flow associated with cyclonic circulations. However, Schultz and Schumacher (1999) recommend usage of the geostrophic wind, as the full wind is not used extensively in the literature. The first term of the equation represents the vertical wind shear and the horizontal temperature gradient. When vertical wind shear is large, as in the baroclinic atmosphere, this term is negative. The second term represents the absolute vorticity of the wind and static stability, and is normally positive, but smaller in magnitude than vertical wind shear. For this reason, EPV tends to be negative.

Negative values of EPV are associated with CSI. A necessary condition for the release of CSI is layer saturation. For this reason, EPV is usually calculated in regions that feature high relative humidity (> 80%). Nicosia and Grumm (1999) have noted a "synergistic" relationship between frontogenesis and EPV which can contribute to enhanced mesoscale snow bands. In practice, the ageostrophic circulation created by frontogenesis increases the horizontal thermal gradient, reducing EPV. With sufficiently low EPV, CI is released, strengthening the updrafts in the mesoscale bands, enhancing snowfall.

Role of Slantwise Convective Available Potential Energy (SCAPE)

Convective available potential energy (CAPE) is a standard measure of parcel instability used in a variety of meteorological applications. On a standard skew-T log-P diagram, the surface-based parcel is traced to the level of free convection and then lifted along the saturation adiabat. The parcel is followed

from level of free convection to the equilibrium level, and CAPE is present in areas between the lifted parcel curve and the environmental sounding. CAPE is represented mathematically as

$$\text{CAPE} = \int_{LFC}^{EL} R_d \left(T_{vp} - T_{ve} \right) d\ln p \, ,$$

where R_d is the gas constant for dry air, T_{vp} is the virtual temperature of the lifted air parcel, T_{ve} is the virtual temperature of the surrounding environment, and p represents the isobaric pressure level. Positive values of CAPE are suggestive of instability capable of creating vertical updrafts. Convective inhibition (CIN) acts to suppress a parcel from rising to the level of free convection where CAPE can be accessed. It should be emphasized that parcel theory does not account for the sizes of the updrafts, entrainment from surrounding air, or the effects of hydrometeors on the environmental sounding. These limitations of parcel theory, in addition to CIN, can explain why regions of positive CAPE can exist in the absence of convection.

Emanuel (1983) has shown that the traditional definition of CAPE can be applied to inertial and gravitational forces on an ordinary skew-T log-P to measure slantwise convective available potential energy (SCAPE). Unlike CAPE, which is concerned with gravitational instability, SCAPE factors in inertial instability as well, and is a measure of the energy available for a parcel to rise unassisted along a slantwise surface. If the environmental CAPE is higher than SCAPE, then vertical updrafts will be the primary convective mode. SCAPE has been observed in a variety of extratropical cyclones, and has been associated with the deepening of these systems (Glinton et al. 2017; Chen et al. 2018).

To calculate SCAPE, the M_g surfaces are determined orthogonal to the thermal wind vector, and then temperature and humidity profiles are interpolated along the M_g surface. In purely barotropic environments, SCAPE is equal to CAPE as the M_g surfaces are orthogonal to the ground. SCAPE is calculated from the slantwise LFC to the slantwise EL, given by

$$\text{SCAPE} = \int_{LFC}^{EL} \frac{g}{\theta_v} \left(\theta_{vp} - \theta_v \right) dz,$$

where θ_v is the environmental potential temperature and θ_{vp} is the temperature of the parcel. Like CIN, slantwise convective inhibition (SCIN) represents the downward energy that the parcel must overcome into order to access SCAPE. Alternative calculations for SCAPE follow parcels as they move along 3D time-evolving M_g surfaces (Gray and Thorpe 2001), but this technique can be computational expensive for large datasets. Three-dimensional SCAPE can also be calculated from the intersection of two pseudoangular momentum components in the x and y direction along sloping surfaces (Gray and Thorpe 2001; Glinton et al. 2017).

Types of Snowbands

Novak et al. (2004) famously classified dozens of Northeast U.S. snow band cases from the period of 1995 to 2001 into single and multi-band types using radar composites. Snow bands were classified into single, multi, or narrow cold frontal bands if they existed for at least two hours. Single bands were the predominant band type and found in nearly 30% of the cases. Narrow cold frontal bands located near the surface cold front or warm sector, occurred in over 20% of the cases. Multi-band events, defined by three or more bands with similar spatial orientation, were less common and occurred in just under 20% of the cases. The remaining 25% failed to meet the above requirements due to shortness of the events and 5% were unclassifiable.
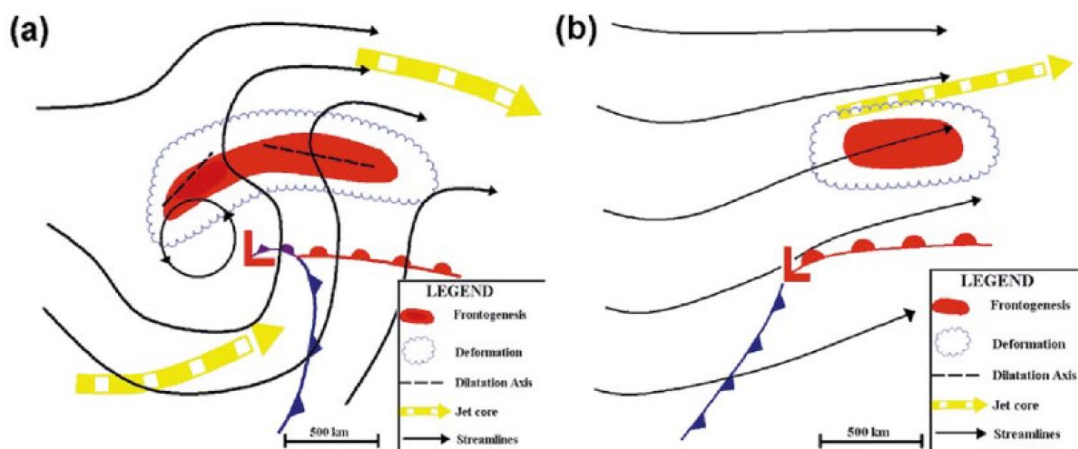
Figure 7: *Schematic of the key environmental differences between (a) single-banded events and (b) nonbanded events. Single-banded events are characterized by a double-jet structure, which places the surface low within the confines of favorable upper divergence. This strengthens the surface and mid-level circulation (indicated by the closed cyclonic streamlines). The frontogenesis is stronger in single-banded events and wraps around northwest of the surface low center. Nonbanded events feature a single jet structure with a weaker surface and midlevel circulation along with weaker frontogenesis. Figure from Novak et al. (2004).*

Most of the single bands are found in the northwest quadrant of the surface low center oriented southwest to northwest in line with the thermal wind vector (Novak et al. 2004). Radar data indicate that these bands exist over short time scales and readily dissipate and redevelop over the same location (Novak et al. 2004). Single bands are more likely to pivot cyclonically around a single point, which can produce large amounts of snowfall in a short period of time. The single band is characterized by a robust midlevel deformation zone that acts on the thermal wind gradient to produce strong midlevel frontogenesis in accordance with the developing warm sector (Figure 7; Novak et al. 2004). Cross sections reveal that

regions of negative EPV exist along the mean band position, favoring moist symmetric stability and slantwise ascent. Nonbanded cases feature weaker frontogenesis and larger conditional stability, resulting in weaker updrafts over a broader region. Multiband events also occur in environments of negative EPV, but have been seen to rearrange into a single band event.

<u>Resolvability of Snow Bands in NWP Models</u>

Slantwise circulations in the presence of moist symmetric instabilities are resolvable in NWP models of high enough resolution. Using a grid spacing of 0.926 km, Fantini et al. (2012) simulated slantwise circulations using a nested non-hydrostatic model. Their simulations supported Morcrette and Browning (2006) who found that slantwise circulations develop from momentum anomalies, referred to as delta-M adjustment. Early in the simulations, anomalies develop along the M surfaces in response to upright convection, which cause a "buckling" of M surfaces with height (Fantini et al. 2012). These buckled M surfaces are flattened due to inertial adjustment from the simultaneous creation of the slantwise circulation (Fantini et al. 2012). It is theorized from Morcrette and Browning (2006) that the delta-M adjustment preconditions the environment for the development of two different regions characterized by moist and dry symmetric instabilities. However, Fantini et al. (2012) found no distinction between these regions, a finding the authors attribute to the similarities between symmetric and inertial instability.

While numerous studies have examined the role of SCAPE in large-scale processes, such as the development of extratropical cyclones, few studies have examined how SCAPE factors into the development of mesoscale snow bands, and even fewer have examined how these findings vary across operational NWP models. Using this brief summary of the prior literature, we proceeded to accomplish the goals set out earlier on improved subjective and objective identification of bands, providing a climatology of those bands and band types, understanding the meteorology varying among those band types, and quantifying their predictability.

<u>Winter Storm Cases</u>

First, northeast U.S. winter storm cases were carefully selected from the large database provided by the Northeast Snowfall Impact Scale (NESIS), which has classified the intensity of over 500 winter storms within the contiguous U.S. from 1900 to present (Kocin and Uccellini 2004). NESIS classifies winter storms on a categorical scale from 1-5, with 5 being the most severe, depending on the magnitude, areal coverage, and population size impacted by snowfall (Kocin and Uccellini 2004). Thus, major snowstorms in large urban areas are more likely to receive a higher NESIS ranking. Potential cases were identified from the NESIS database unrelated to their ranking but based on their accessibility within the contiguous U.S. GridRad composite of over 100 Next-Generation Radar (NEXRAD) sites spanning 1995-2017.

Furthermore, potential cases must have existed within the archival period of modern operational NWP forecast data, which roughly began in 2004. These two time-based constraints alone reduced the number of potential cases to 131 winter storm events.

To further narrow down the number of potential cases and eliminate events located in other regions of the U.S., the Northeast U.S. was divided into 16 equally sized boxes oriented parallel to the coast (Figure 8). Precipitation within all boxes can be attributed to mid latitude cyclones; however, boxes 1-4 may see contributions from lake effect sources. Boxes 5-8 are located far enough inland that lake effect snow contributions are marginal, while boxes 13-16 are located too far offshore to have any weight in the filtering of this case list. Boxes 9-16 feature major metropolitan areas and often see considerable amounts of snowfall during winter storms. Therefore, all future filtering utilized boxes 9-14. Radar reflectivity values were studied within these boxes for the remaining 131 cases.
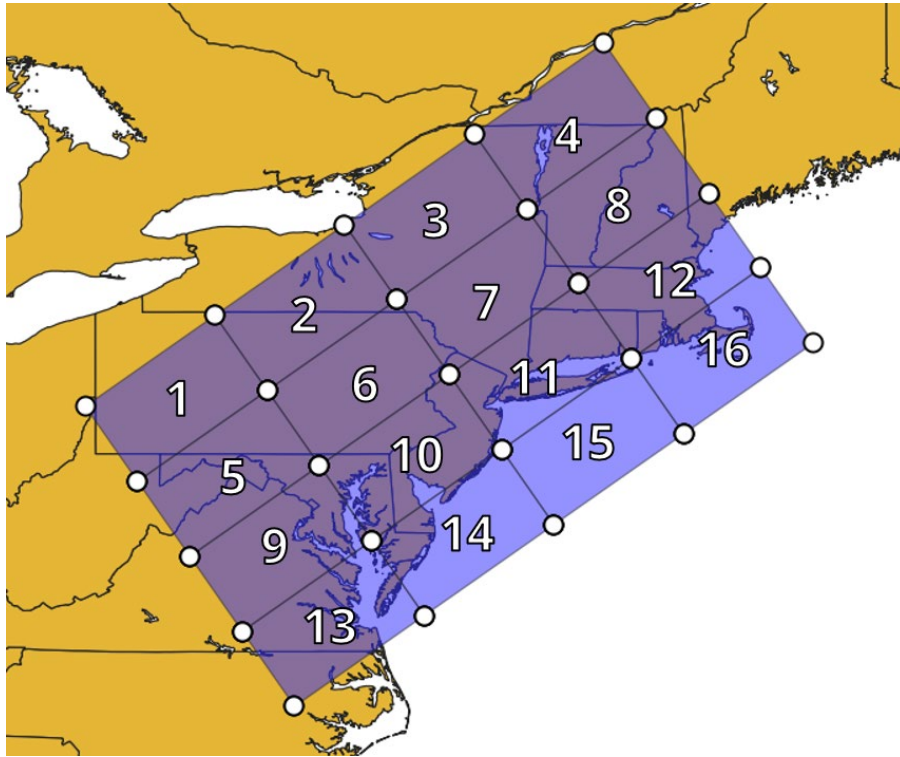
Figure 8: *Equally sized boxed regions used to filter the NESIS winter storm cases. Boxes 9-12 are of most interest because they feature major cities and often experience high impact winter storm events with a variety of precipitation types.*

While ground observations often lack spatial uniformity, radar provides reliable and frequent sampling of entire precipitation regions. This allows for the assessment of winter storm intensity as well as duration. The combination of several radars in the form of a composite provides complete coverage of a

region by reducing the effects of beam blockage from terrain, trees, or even buildings. Composite radars also address issues associated with 'blackouts' when a single radar site goes offline, a problem frequently seen in intense storms. GridRad, a sophisticated new composite radar dataset, provides gridded 1-hourly 0.02° x 0.02° x 1 km radar data of the eastern U.S. from 1995 to 2017 (Homeyer and Bowman 2017). In boxes 9-14, time series of average GridRad reflectivity values were produced to determine the intensity and duration of the NESIS winter storms. Because GridRad does not differentiate frozen precipitation from pure rain, the average 500-1000 mb thickness was calculated in each box using the North American Regional Reanalysis (NARR), a 3-hourly 0.3° high resolution reanalysis dataset with coverage available from 1979 to present for all of North America (Mesinger et al. 2006).

The final level of filtering requires that average reflectivity within any of the boxes 9-12 be >10 dBZ while average 1000-500 mb thickness be <5400 m for at least six hours. This process eliminated weak storm cases and events which might be contaminated from radar artifacts such as ground clutter. Short duration events were eliminated as well as any event where snow is not the dominant precipitation type. This ensures that the winter storm cases have a strong enough signal to appear in operational models with coarse grid spacing. Finally, this filtering removed cases located outside of the northeast U.S. Additional quality control was performed to eliminate duplicate events. This reduced the number of Northeast U.S. winter storm cases to 46 events from 2004-2016 (Table 4).

12/20/2004	12/19/2009	1/11/2011	2/12/2014
1/5/2005	12/31/2009	1/26/2011	3/2/2014
2/28/2005	1/30/2010	2/21/2011	3/15/2014
2/11/2006	2/2/2010	2/26/2011	1/26/2015
2/13/2007	2/5/2010	10/28/2011	1/30/2015
2/21/2008	2/9/2010	2/8/2013	2/2/2015
12/19/2008	2/15/2010	3/6/2013	2/8/2015
12/21/2008	2/23/2010	3/18/2013	2/14/2015
1/10/2009	2/25/2010	3/25/2013	2/16/2015
2/22/2009	3/2/2010	12/14/2013	1/22/2016
3/1/2009	3/3/2010	1/2/2014	
11/27/2009	12/26/2010	1/21/2014	

Table 4: *Start date of winter storm cases that featured at least six hours of snow within the Northeast U.S.*

Forecast Datasets Used

The predominant operational forecast models for the contiguous U.S. are the Global Forecast System (GFS) and the North American Mesoscale Forecast System (NAM). The GFS has existed under different pseudonyms since its inception in August 1980 as the Global Spectral Model (GSM), later becoming the GFS Aviation (AVN) model, and then the GFS Medium Range Forecast (MRF) model. Nearly 40 years later, the GFS has undergone multiple upgrades to its dynamical core and physics parameterizations with increasing vertical levels and finer grid spacing. The NAM was first introduced as the Meso-ETA model in June 2003 with 3 different horizontal resolutions and boundary conditions provided by the GFS. The NAM has also seen advancements in its vertical and horizontal grid spacings with improved model physics. Additional details about the GFS and the NAM are provided in the subsections below.

The GFS provides global forecasts at a horizontal resolution of 0.5° with 64 vertical levels four times daily at 00, 06, 12, and 18 UTC. Model output is available in 3-hourly intervals up to 192 hours out. Archival data for the 0.5° GFS is available online from NOAA's National Center for Environmental Prediction (NCEP) from 10 October 2006 to present, while data for the 1° GFS is available from 15 February 2005 to present (NCEI 2020a). Only four winter storm cases in Table occurred before 10 October 2006 and feature the 1° GFS. In June 2019, the GFS was upgraded to the Finite-Volume Cubed-Sphere (FV3) dynamical core, which replaced the spectral dynamical core of the previous version (Otto and Thornton 2020a).

The NAM was originally named the Meso-ETA model, but was changed to its current name in 2005 (NCEI 2020b). At its core, the NAM uses the non-hydrostatic version of the Weather Research and Forecasting (WRF) model with 60 vertical levels (NCEI 2020b). Boundary conditions for the NAM are provided by 6-hour old GFS forecasts. The 12 km NAM also provides boundary conditions to four 3 km nested domains over the continental U.S., Alaska, Hawaii, and Puerto Rico, which provide high resolution model output up to 60 hours out (Otto and Thornton 2020b). The 12 km NAM provides regional forecasts for North America four times daily at 00, 06, 12, and 18 UTC in 3-hour intervals up to 84 hours out. Archival data for the 12 km NAM is available from NOAA's NCEP from 20 June 2006 to present (NCEI 2020b). This means that the four earliest winter storm cases listed in Table lie outside the NAM record. The last major update to the NAM occurred in 2017. Eventually the NAM will be phased out in favor of a high resolution standalone version of the GFS-FV3 (Otto and Thornton 2020b).

Cross Sections Developed

Traditional proxy-based methods for diagnosing the potential for slantwise convection are evaluated on cross sections oriented perpendicular to the thermal wind vector, which can be approximated using the thickness contour. Moore and Lambert (1993) used the 850-300 mb thickness field to study a significant snow event over Missouri. The methodology in this document utilizes the 1000-500 mb thickness field instead; however, the 850-300 mb thickness is likely smoother as it does not incorporate surface layer effects or extrapolation below ground. Regardless of the thickness layer used, older studies have all selected cross section start and end points by hand, a process that is tedious and subjective. A novel approach is presented in this proposal by evaluating cross sections everywhere perpendicular to the thickness field. This allows for vertical values to be consolidated onto horizontal points which can be mapped onto plan view plots.
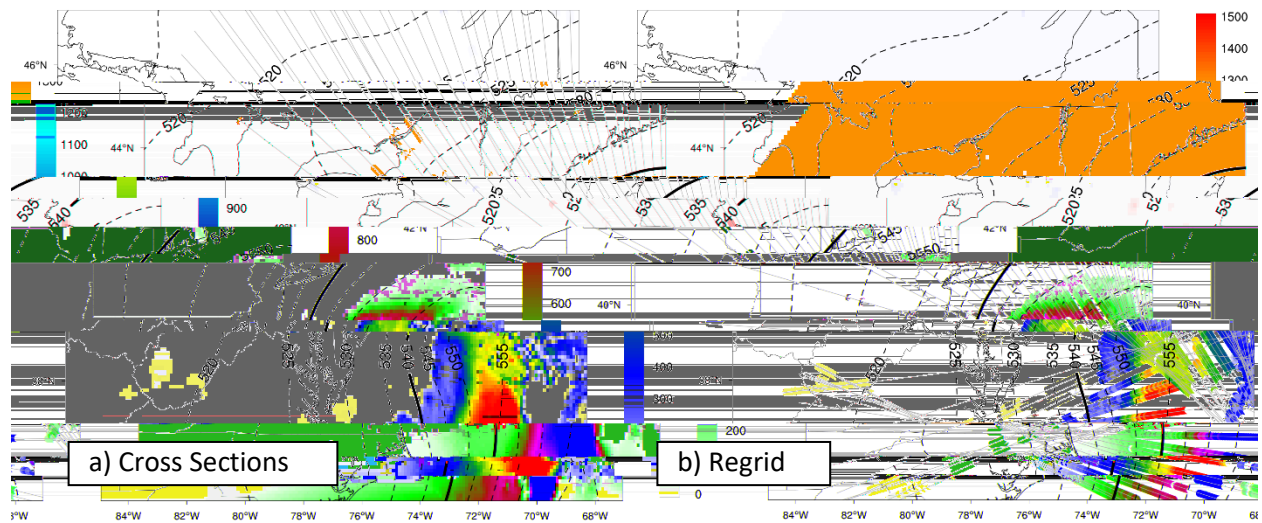
Figure 9: *Comparison of (a) randomly spaced data points from multiple cross sections oriented perpendicular to the 540 dm 1000-500 mb thickness contour (solid black line) and (b) the same data points remapped onto a 0.1° x 0.1° equally spaced grid for the NAM. The individual cross sections in (a) are outlined in light grey. The values displayed are SCAPE (J/kg).*

Cross sections spanning 10° with 250 horizontal points are centered orthogonal to all possible paths of the 1000-500 mb 540 dm thickness contour. For the GFS, the cross sections incorporate over 20 data points, while the NAM has close to 100 data points along the cross-section axis. An example of this methodology for the NAM is shown in Figure 9a. The usage of multiple cross sections reveals the locations of high SCAPE along the cold front of a mid-latitude cyclone located off the coast of New Jersey. Still, there are gaps in the data coverage over parts of the warm sector, and there are intersecting contours in

some parts of the map. To combat these issues, the randomly spaced data points from the cross sections are remapped onto a 0.1° x 0.1° equally spaced grid using natural neighbor interpolation (Figure 9b). The grid spacing of the remapped data is high enough to capture the across variation in SCAPE along the cross section, and the interpolation fills in the missing regions and averages out the intersecting values. However, artifacts are present over the southern part of the domain located away from the cross sections.

<u>Calculations of equivalent potential vorticity and frontogenesis</u>

Along each cross section, saturated EPV is calculated according to Moore and Lambert (1993) and Nicosia and Grumm (1999) using geostrophic momentum (M_g) surfaces and saturated equivalent potential temperature (θ_{es}). Geostrophic momentum is defined by $M_g = V_g + fx$, where V_g is the geostrophic wind and f is the Coriolis parameter. There is debate at large regarding the usage of geostrophic versus the full wind when calculating EPV (Schultz and Schumacher 1999). Novak et al. (2004) argue that usage of the full wind is more representative of the curved flow associated with cyclonic circulations. Regardless, EPV is described as

$$\text{EPV} = g \left[\left(\frac{\partial M_g}{\partial} \right. \right.$$

are characterized by frontogenesis, while areas experiencing a weakening of temperature gradients are in frontolysis.

Calculation of SCAPE

Emanuel (1983) has shown that SCAPE can be calculated along M_g surfaces using traditional Skew-T/Log-P diagrams for diagnosing CAPE along isobaric levels. The less slanted the M_g contour, the more barotropic the atmosphere, and SCAPE can be approximated more closely to CAPE. M_g surfaces are computed along every cross-sectional point beginning at the 1000 mb level. If the M_g surface folds with height, the parcel is said to be inertially unstable, and SCAPE is not calculated along this M_g surface. For now, SCAPE is only calculated along M_g surfaces that extend from the 1000 to the 400 mb layer. In the future, this rule might be relaxed to include parts of the M_g surface which have not folded with height. The temperature and dew point are retrieved from each M_g surface and SCAPE is computed in the traditional sense of CAPE. SCAPE is calculated using the NCAR Command Language (NCL) CAPE function, which approximates the value of positive buoyant CAPE using the read/interpolate/plot (RIP) method. SCAPE is calculated along all vertical levels of the M_g surface, and any preliminary results from here on out depict the maximum unstable SCAPE of the layer. In the future, this calculation might be adjusted to calculate the mean-layer SCAPE of the lowest several hundred millibars of the troposphere.

All cases examined will be summarized in the Ph.D. dissertation of Mark Nissenbaum. However, for brevity, a single case study is presented here for the 27 December 2010 winter storm, which dropped widespread snowfalls between 12 and 32 inches across much of the northeast U.S. The snowfall varied spatially over the region due to the persistence of several unique and dominant snow bands. Early on the 27 December, a large arched snow band with intense snow fall rates pivoted over the eastern New Jersey and New York City with multiple weaker bands located offshore of New Jersey parallel to the 540 dm thickness contour (Figure 10). In the end, eastern parts of New York City received as much as 30 inches of snow, while neighboring areas to the west received considerably lower amounts.

A comparison between GFS and NAM 850-700 mb minimum EPV is presented in Figure 11. The placement of the surface low centers is similar between the two models, but the NAM has initialized with a slightly deeper low, possibly due to the finer grid spacing of the NAM. Both models have initialized the two main bands of EPV arched over New Jersey and areas immediately offshore. This placement of the EPV over New Jersey coincides with the single band on the reflectivity in Figure 10. The NAM (Figure 11b) did not resolve the EPV southwest of the low center nor south of Maine. It is possible that instead the NAM has released the slantwise instability through other means. The EPV and frontogenesis coexist northwest of the low center, similar to the findings from Nicosia and Grumm (1999) in their case studies of northeast winter storms. Despite the strong frontogenesis over eastern Connecticut, there is an absence of

19

EPV in this area. Since frontogenesis slopes with height, it is possible that the EPV and frontogenesis coexist at lower levels.

A comparison between GFS and NAM CAPE is presented in Figure 12. The NAM (Figure 12b) has resolved considerably much more CAPE than the GFS (Figure 12a). These differences might again be related to the horizontal and vertical grid spacings of the models. The location of the CAPE makes sense within the warm sector of the midlatitude cyclone. Interestingly, CAPE values of roughly 500 J kg^{-1} coexist within the offshore frontogenetical region. It is possible that the strong frontogenesis has increased CI by strengthening the temperature gradient. There were multiple precipitation bands present in this region of high CAPE and frontogenesis (Figure 10). It seems unlikely that these offshore bands were due to CSI with such high values of CAPE

A comparison between GFS and NAM SCAPE is presented in Figure 13: with SCAPE-CAPE differences shown in Figure 14. The orientation of the SCAPE along the cold front wrapping into the surface low is consistent between the two models. The appearance and magnitude of the SCAPE values is similar to the case studies presented in Glinton et al. (2017) for extratropical cyclones located over the north Atlantic. The NAM (Figure 13b) once again resolved higher values of SCAPE, possibly due to the finer resolution of the model. In the NAM, the SCAPE is higher in the vicinity of the surface low, although this could be a side effect of the more deeply initialized surface low. The SCAPE-CAPE differences in Figure 14 reveal where SCAPE is more dominant and slantwise convection is likely to take place. Once again, the cold front is characterized by very large values of SCAPE in comparison to CAPE. What is also interesting is the placement of SCAPE near the center of the low with strong frontogenesis immediately to the northwest. It is possible that the neighboring regions of SCAPE and CAPE/frontogenesis are no coincidence, but a result of the ageostrophic thermally direct circulation.

With the database of banding events identified, and the ability to calculate several metrics including SCAPE, we next proceeded to develop a methodology for identification of the individual bands within each event such that we could calculate the climatology of band frequency, structure characteristics, and also to allow compositing based on those characteristics. These are all described next.
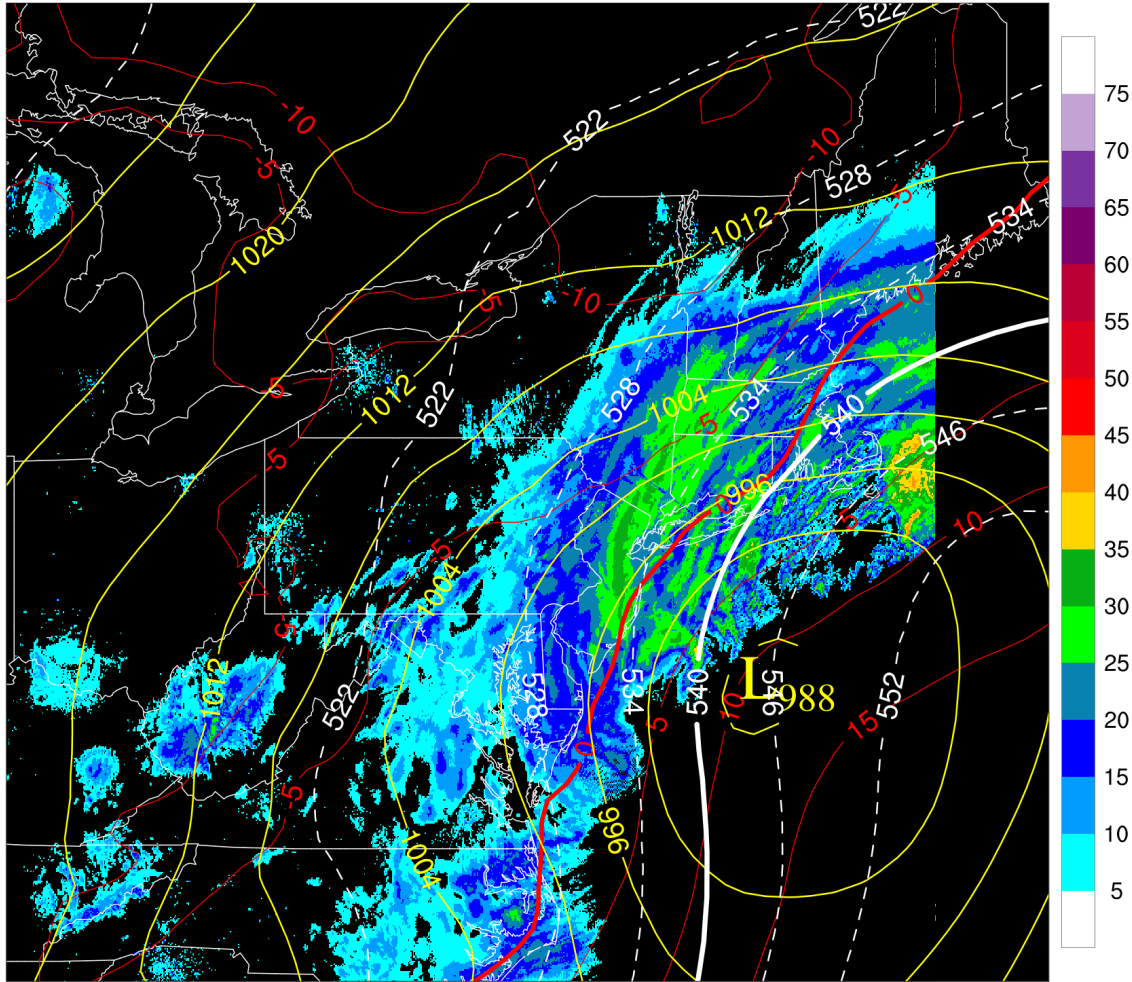
Figure 10: *GridRad reflectivity (dBZ, shaded) valid at 00 UTC 27 December 2010 overlaid with NARR 1000-500 mb thickness (dm, dashed white; 540 dm line solid white), mean sea level pressure (mb, solid yellow), and 2 m air temperature (°C, red; freezing line in bolded red). A large banded feature is present over western Massachusetts into New Jersey, assumed to be all snow since it is below the freezing line. Smaller banded features are seen offshore, while precipitation over coastal Massachusetts is more intense and convective in nature.*
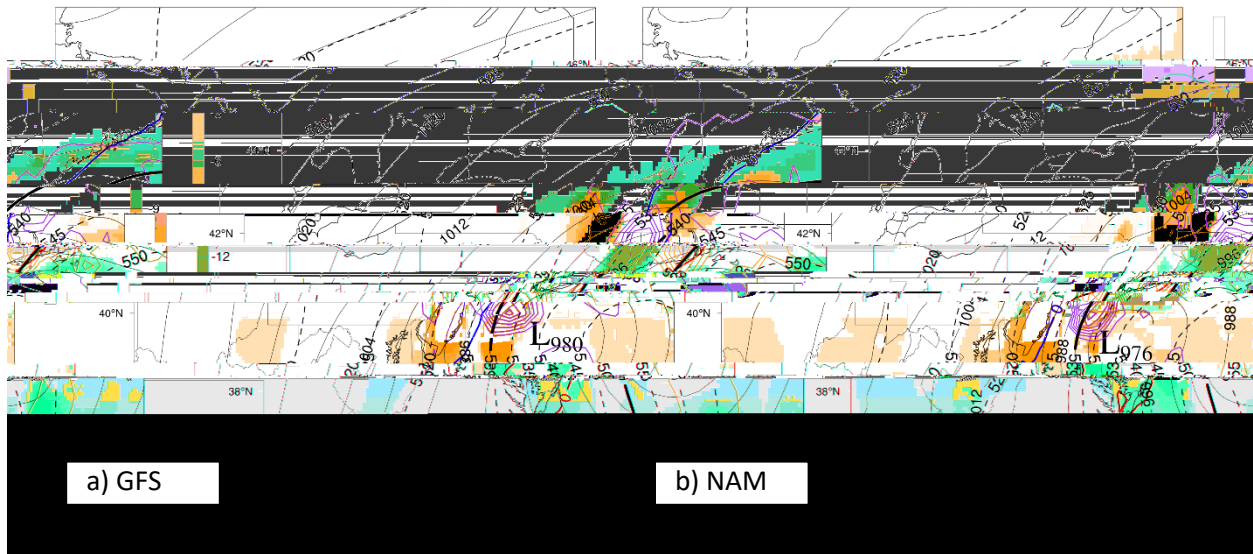
Figure 11: Comparison of (a) GFS and (b) NAM 850-700 mb minimum EPV with relative humidity greater than 80% (x 10^{-7} K Pa s^{-1}, shaded), 850-700 mb geostrophic frontogenesis (intervals of 1 K 3-hr^{-1} 100 km^{-1}, purple), 1000-500 mb thickness (dm, dashed; 540 dm line solid), mean sea level pressure (mb, solid), and 2 m 0°C temperature line (blue) at the models' initialization time valid at 00 UTC 27 December 2010.
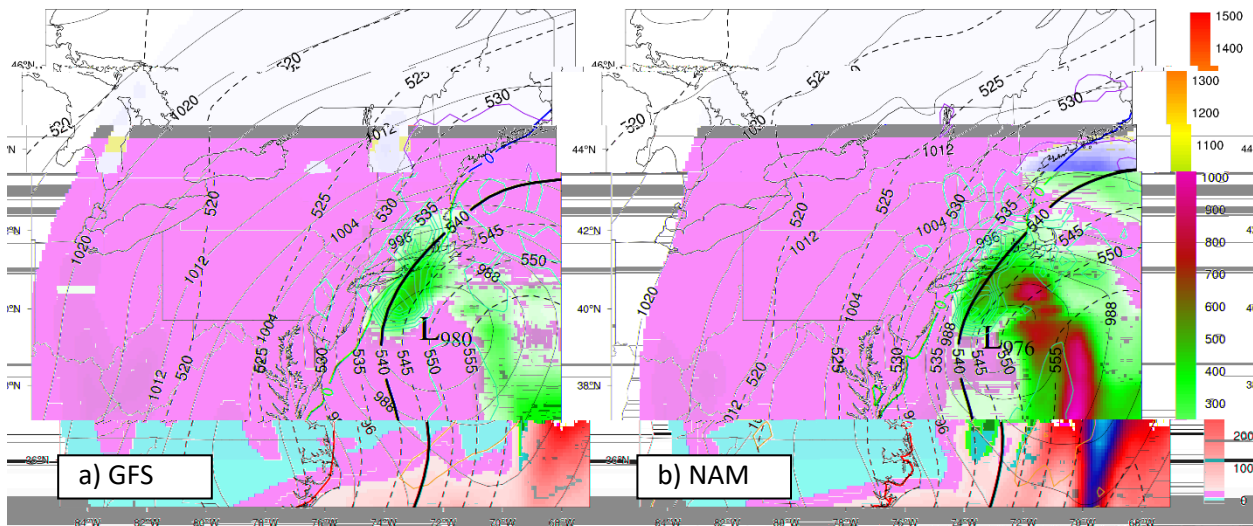
Figure 12: Same as Figure , except CAPE (J kg^{-1}) is shaded instead.
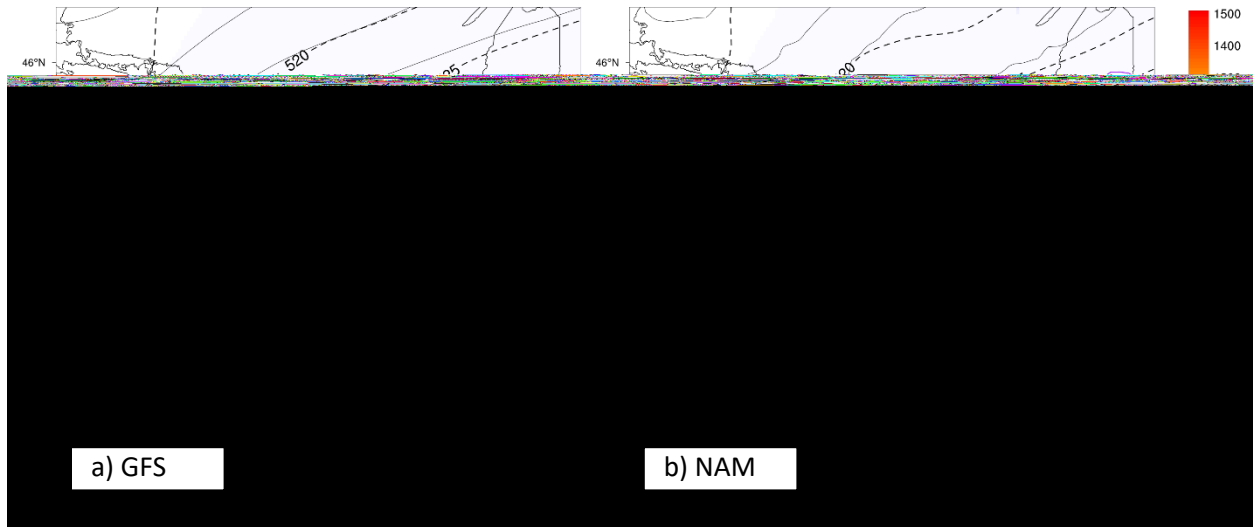
Figure 13: *Same as Figure , except SCAPE (J kg⁻¹) is shaded instead.*
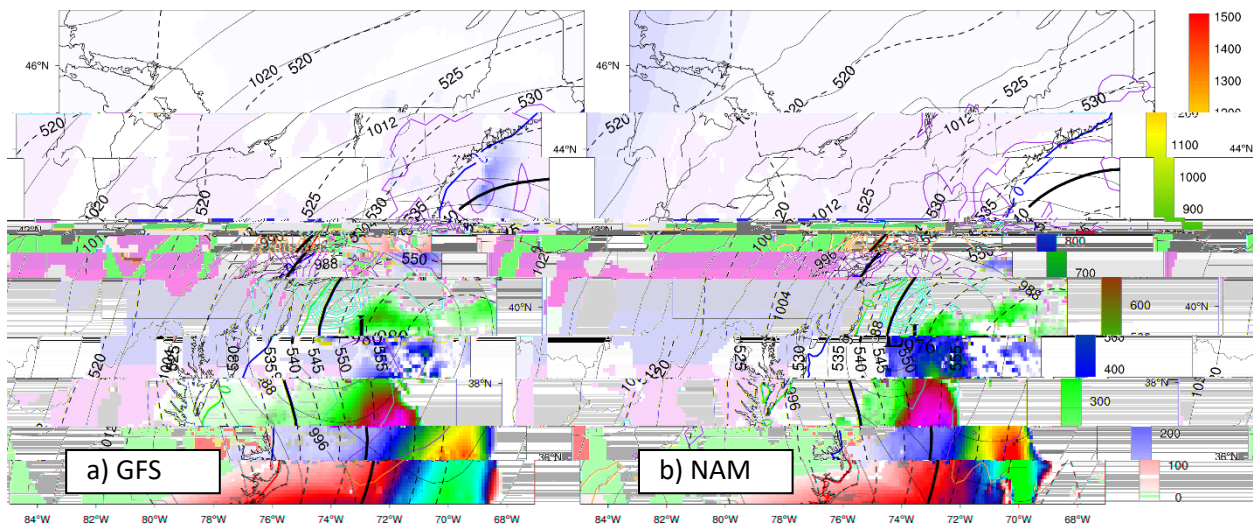
Figure 14: *Same as Figure , except SCAPE-CAPE (J kg⁻¹) is shaded instead.*

Band Identification Methodology

Precipitation bands were manually identified from 3-hourly GridRad composite reflectivity images of the NEUS domain georeferenced into the GeoTiff image format using the Geospatial Data Abstraction Library (GDAL) toolset. GDAL assigns real-world coordinate pairs to point locations within the image's coordinate system. The georeferenced images were imported into QGIS where precipitation bands were

23

identified using the polygon tool. Precipitating regions were declared "band-like" if they contained at least 15 dBZ with notably larger lengths than widths. Under this lenient classification, banded features can take on various shapes and gradations of curvature. All possible bands were identified, including those containing rain, snow, and thunderstorms as GridRad cannot differentiate between precipitation types.

Band Types Categorization

Banded structures exceeding 15 dBZ were classified into either isolated, embedded, broken, fine scale, heavy precipitation, or merged band types, and can include any combination of these types. Banded features were also classified into cold and warm frontal bands, which occurred less often. An example of each of these band types is shown in Figure 15. Embedded bands exist within large precipitation shields, while isolated bands appear to stand alone. Broken bands are segmented but still maintain a banded structure, and heavy precipitation bands contain reflectivity values exceeding 40 dBZ. Multi-bands were differentiated from single bands if two or more bands of similar appearance, shape, and size were oriented parallel to each other. The fine scale band type (Figure 15d) is a form of multi-band, but the precipitation bands are too numerous and segmented to be classified individually.

Band Characteristics Quantification

From the original 45 winter storm cases, only 42 contained identifiable precipitation bands. There were 1095 bands identified in total, with single bands the most common (Figure 16). Most bands tend to be embedded within larger precipitation shields (Figure 17). The high incidence of embedded bands may be from the composite reflectivity that was used to identify banded features. Cold and warm frontal bands were the least commonly observed band type (Figure 17).
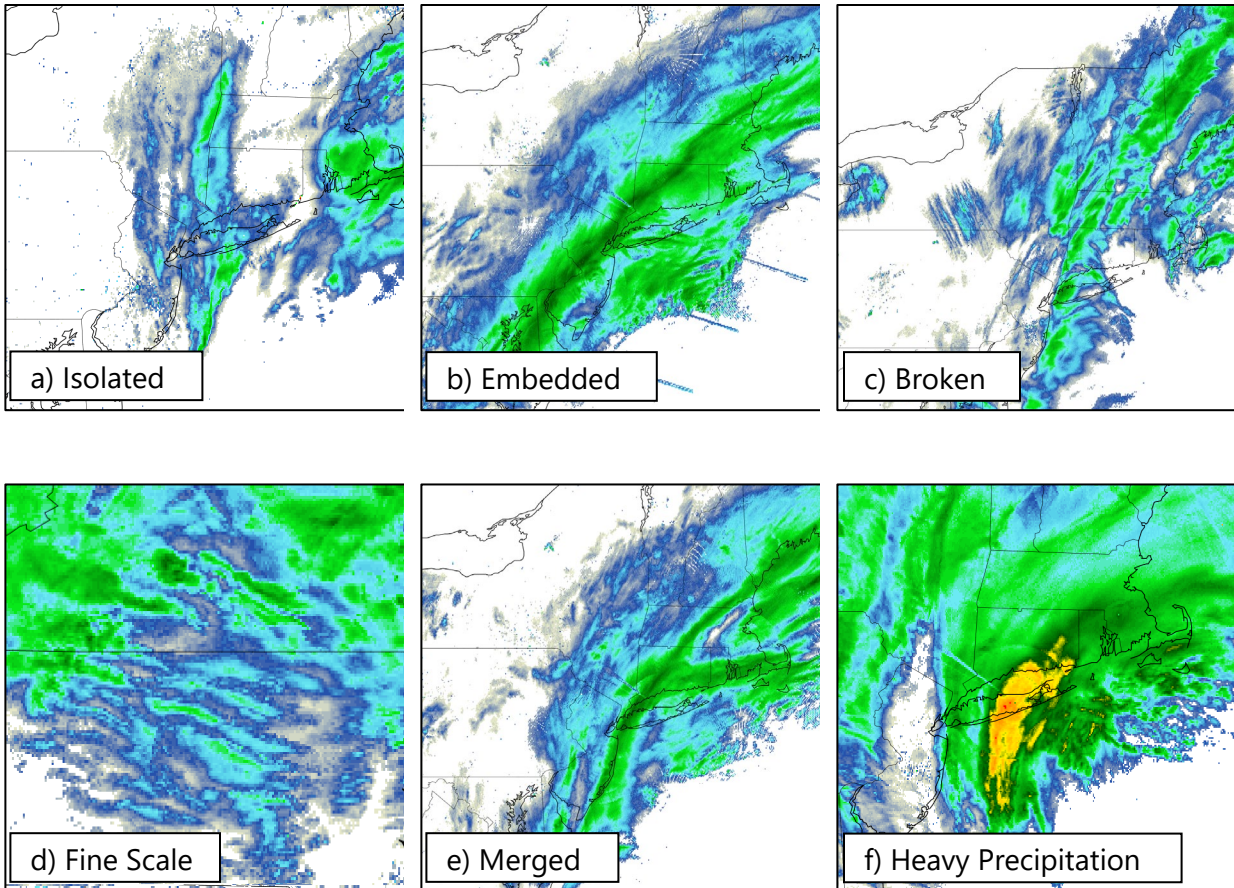
Figure 15: *Example of (a) an isolated band over eastern New York and Long Island on 7 March 2013 at 15 UTC, (b) an embedded band over New Jersey, New York, and neighboring states on 12 February 2006 at 12 UTC, (c) a broken band over Maine, Massachusetts, Connecticut, and neighboring states on 27 December 2010 at 12 UTC, (d) a series of fine scale bands over central North Carolina and southern Virginia on 19 December 2009 at 9 UTC, (e) merged bands over Connecticut and neighboring states on 12 February 2006 at 15 UTC, and (f) a heavy precipitation band over Long Island and eastern Connecticut on 9 February 2013 at 0 UTC.*

Occurrence of Single and Multi-bands
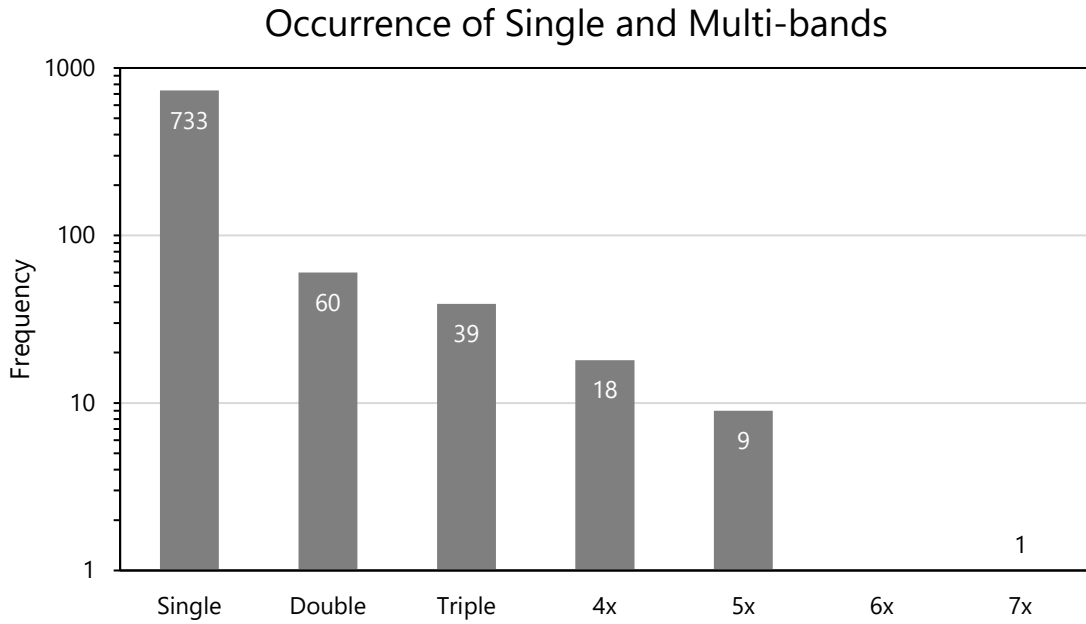
Figure 16: *Frequency of single and multi-bands.*

Occurrence of Each Band Type
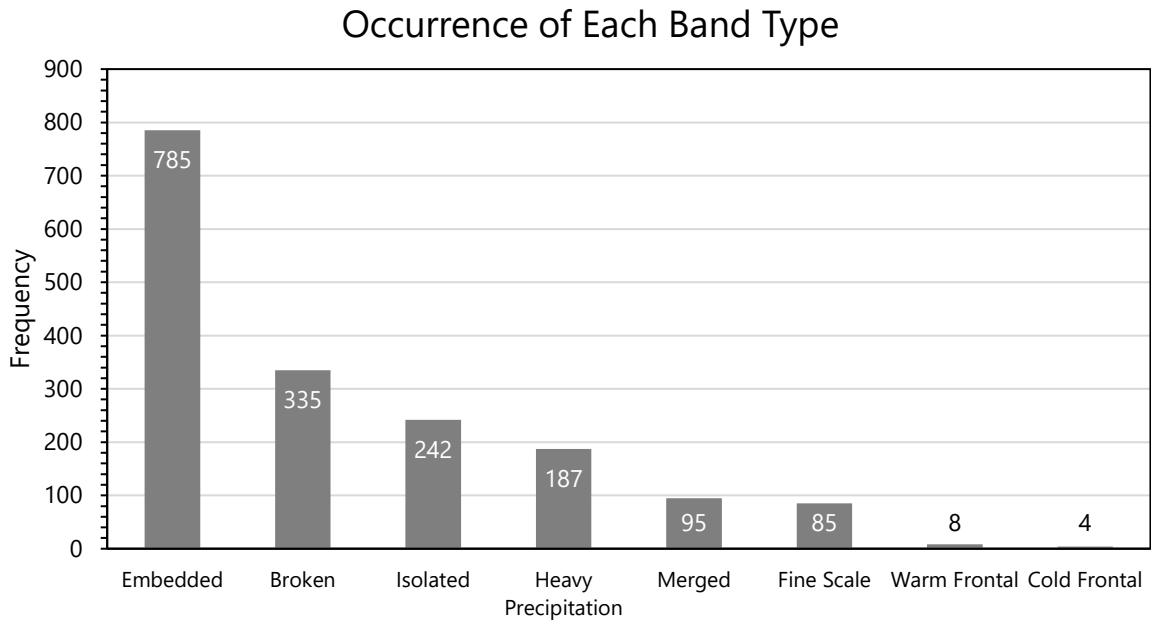
Figure 17: *Occurrence of each band type. Identified bands can belong to more than one category.*

Band Geometry Determination

        Bands typically contain areas <40,000 km^2, with larger bands less common (Figure 18, left). Band perimeters (Figure 18, right) tend to lie between 400-1,200 km and trail off quickly as large perimeters are less common. It should be noted that some bands were cut off over the ocean and in parts of Canada due to the limited extent of the GridRad dataset.

        The oriented minimum bounding box (OMBB) was calculated using the Processing Toolbox in QGIS for each identified band. OMBB determines the minimum area rotated rectangle for each feature, which makes it possible to assess band aspect ratios. The most common band ratio is between 3:1 and 4:1 (Figure 19, left), with most of the dataset featuring band aspect ratios greater than 3:1. This result agrees with Ganetis et al. (2018), which algorithmically identified banded features with a minimum band aspect ratio of 3:1. Band aspect ratios that are close to 1:1 (Figure 19, right) are most likely associated with fine scale bands, as these bands types were "circled" using the polygon tool. Band extent, which is a measure of the band area to the area of its OMBB, is shown in Figure 20 . Band extent can be used as a proxy for band curvature, as curved bands feature larger OMBBs in comparison to the actual band area. Therefore, low values for extent might be associated with curved bands. If the area of the OMBB and the band are equal, then the extent will be equal to 1. The most common band extent is between 0.5-0.6, while values beyond 0.7 are extremely rare. This indicates that most identified bands had some degree of curvature.
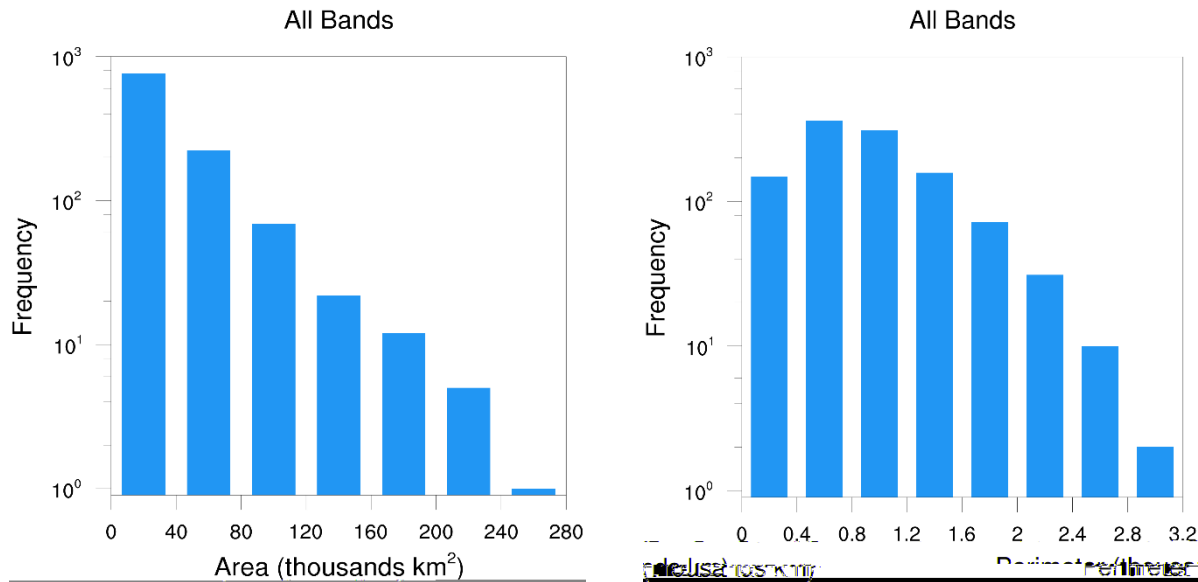
Figure 18: *Frequency of band areas (left) and perimeters (right) for all bands.*
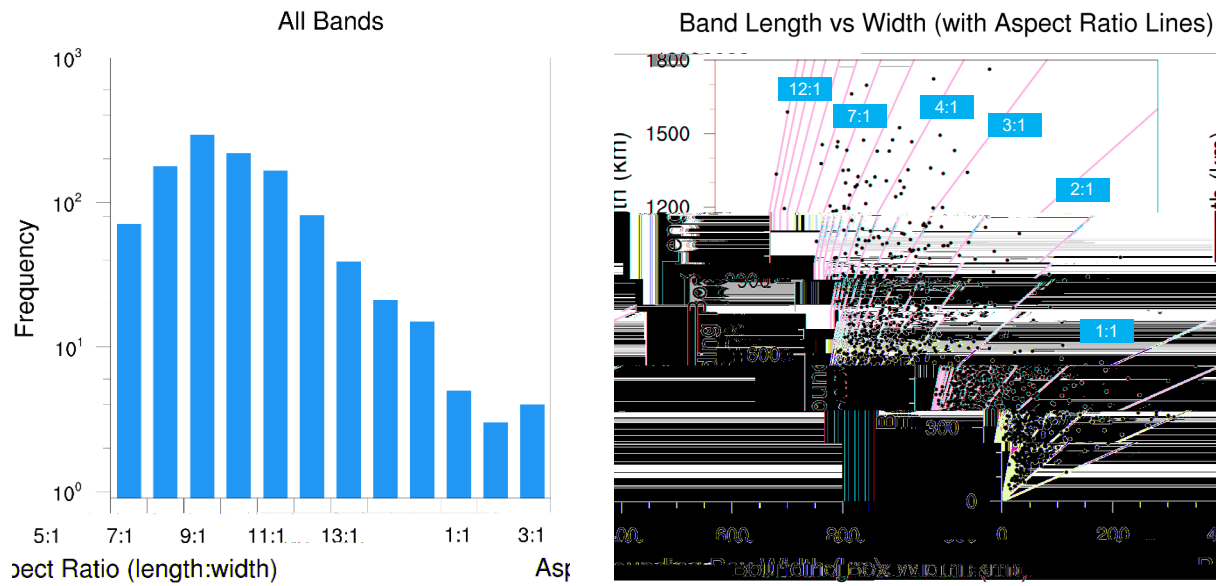
Figure 19: *Frequency of band aspect ratios determined from the minimum oriented bounding box (left) and relation between bounding box width and height (right).*
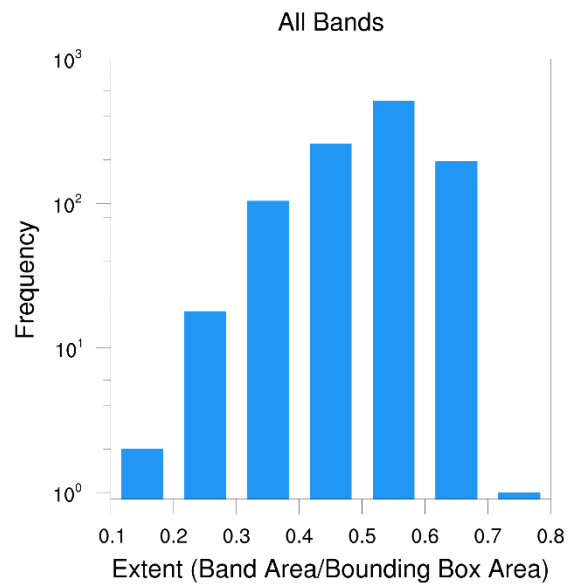

Figure 20: *Frequency of band extent, comparing the area contained by the band itself to that of its oriented minimum bounding box.*

<u>Band Angle Composites</u>

Band angles, calculated relative to geographic north, were determined from the OMBB dimensions (Figure 21). Band angles tend to feature a southwest to northeast orientation (between 0-90°), characteristic of the usual location of bands on the northwest side of mid latitude cyclones. Purely meridional bands were rare, possibly because these bands tend to be weaker and are more likely to be excluded from the winter storm dataset. Composite images of the binned bands in Figure are shown in Figure .

The composite 500 hPa NARR geopotential heights associated with the binned band angles is shown in Figure 22. Bands tend to be located on the eastern side of the composite mean trough oriented roughly parallel to the 500 hPa geopotential height contours, in line with the placement of the surface low. However, there are a few bands which intersect the 500 hPa geopotential height contours on the base and western side of the trough. The largest standard deviations in geopotential height tend to be located at the base of the trough (Figure 23), which might explain the intersecting bands in the composite mean. Band orientation is related to the amplitude of the trough, with a more meridional band associated with a deeper trough.
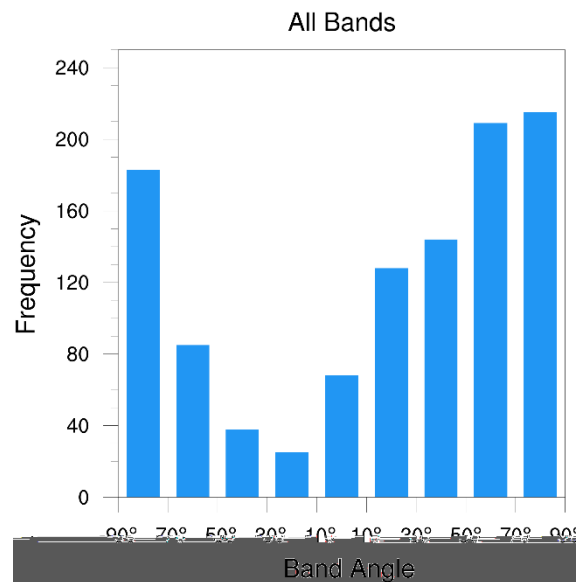
Figure 21: Distribution of band angles, measured in degrees relative to North, determined by the minimum oriented bounding box. Only bands with aspect ratios greater than 4:1 are included. A band angle of 0° is meridional, while angles of 90° are zonal. A southwest to northeast oriented band would have a band angle between 0 and 90°.
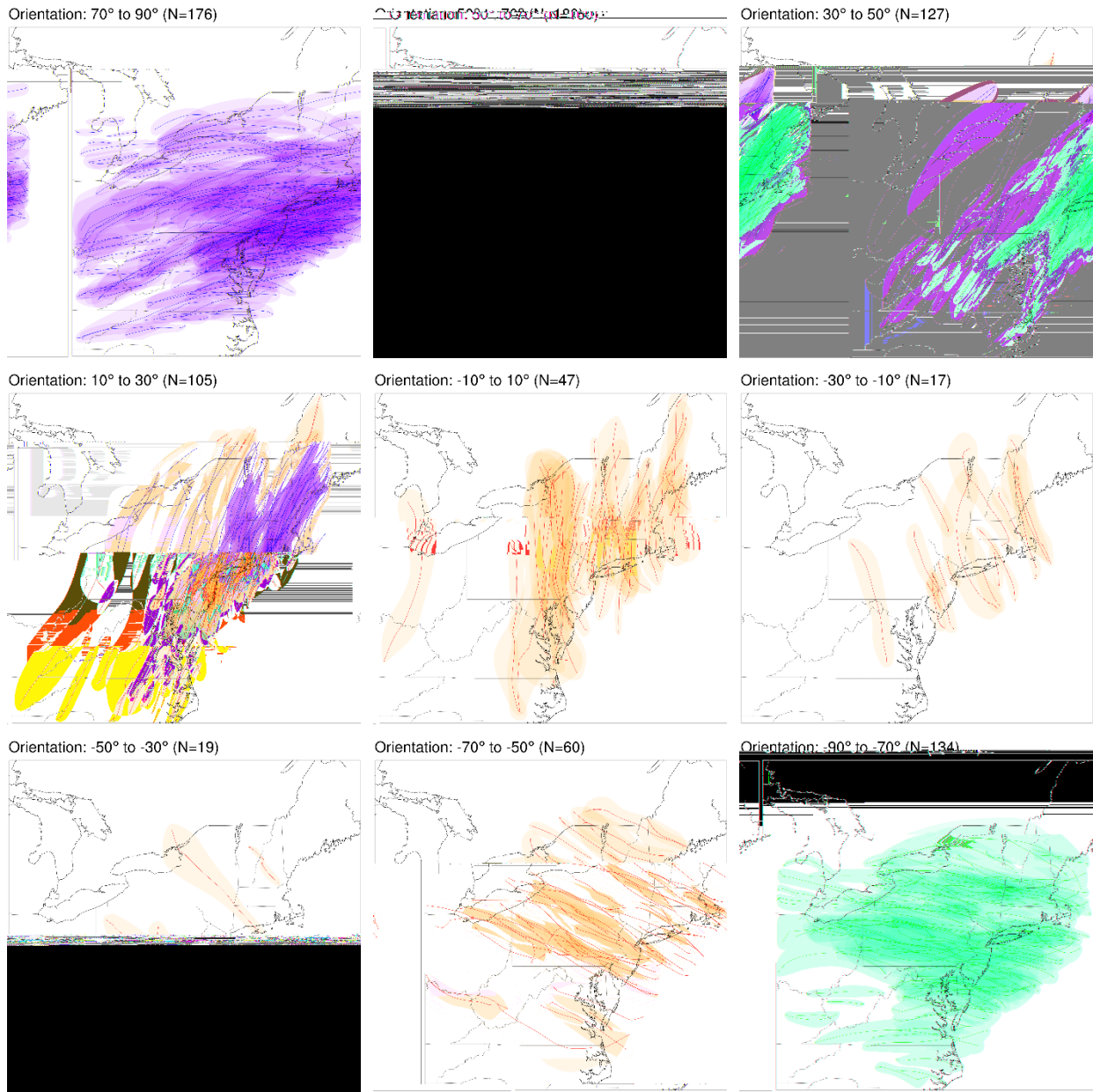
29

Orientation: 70° to 90° (N=176)

Orientation: 50° to 70° (N=180)

Orientation: 30° to 50° (N=127)

Orientation: 10° to 30° (N=105)

Orientation: -10° to 10° (N=47)

Orientation: -30° to -10° (N=17)

Orientation: -50° to -30° (N=19)

Orientation: -70° to -50° (N=60)

Orientation: -90° to -70° (N=134)

Figure 22: *Bands (shaded) and band centerlines (red) composited according to band angle as shown in Figure 21.*

30

Band Angle: 70° to 90° (176 bands from 31 cases)
NARR 500 hPa Composite Geopotential Height (dm)
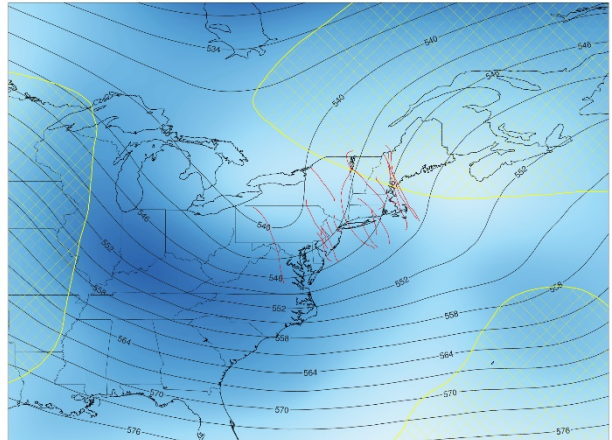with Standard Deviations (m) and <0.01 Significance (hatching)
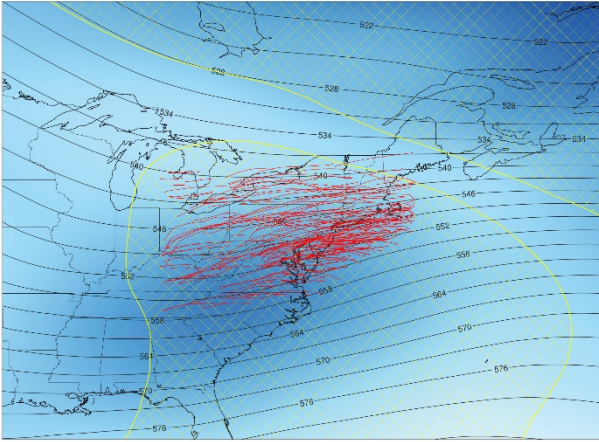
Band Angle: 50° to 70° (160 bands from 32 cases)
NARR 500 hPa Composite Geopotential Height (dm)
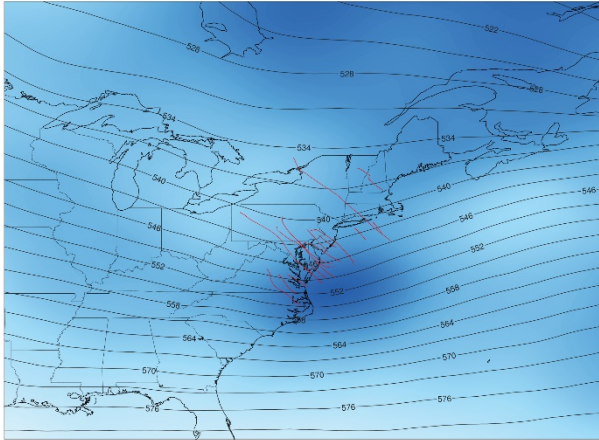with Standard Deviations (m) and <0.01 Significance (hatching)
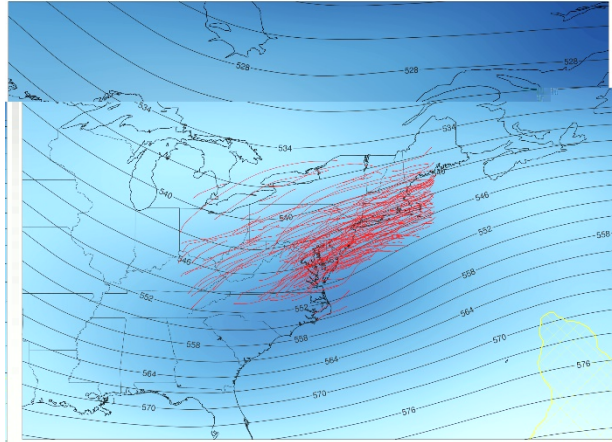
Band Angle: 30° to 50° (127 bands from 31 cases)
NARR 500 hPa Composite Geopotential Height (dm)
with Standard Deviations (m) and <0.01 Significance (hatching)
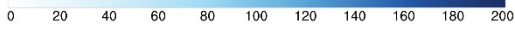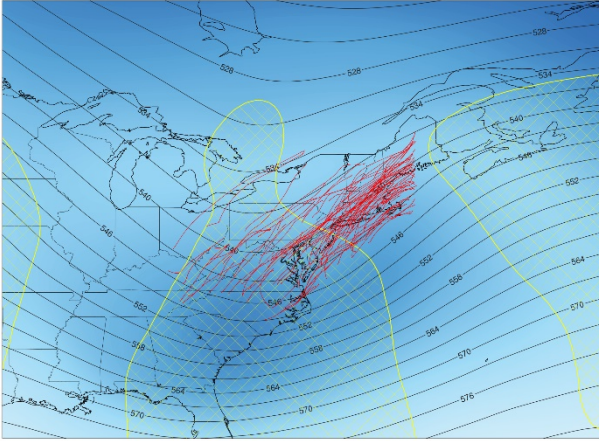
Band Angle: 10° to 30° (105 bands from 28 cases)
NARR 500 hPa Composite Geopotential Height (dm)
with Standard Deviations (m) and <0.01 Significance (hatching)
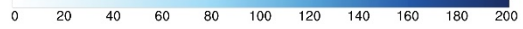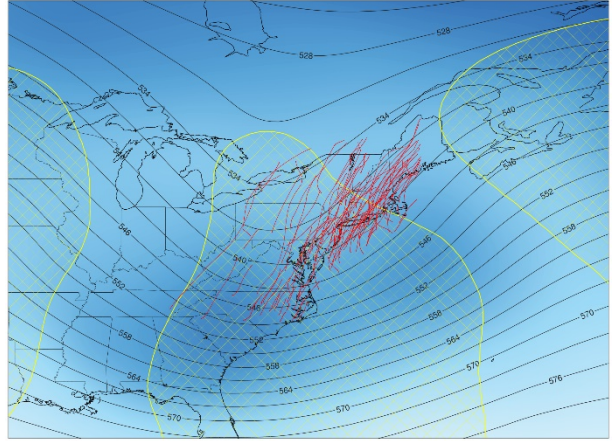
Band Angle: -10° to 10° (47 bands from 16 cases)
NARR 500 hPa Composite Geopotential Height (dm)
with Standard Deviations (m) and <0.01 Significance (hatching)
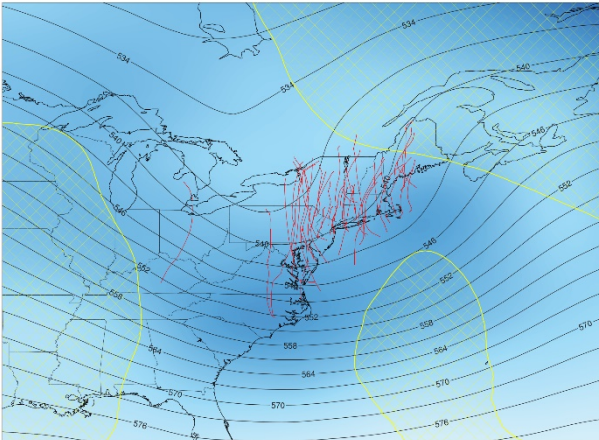
Band Angle: -30° to -10° (17 bands from 8 cases)
NARR 500 hPa Composite Geopotential Height (dm)
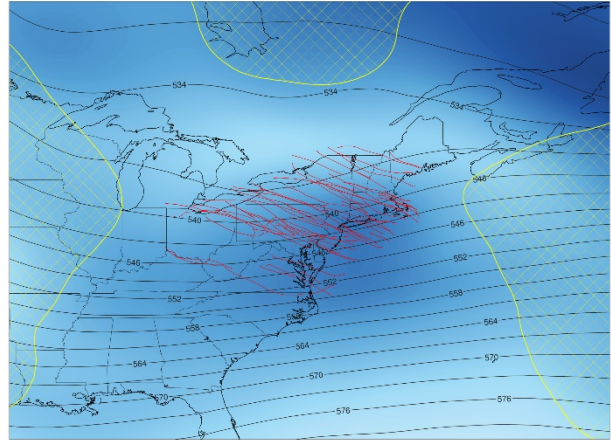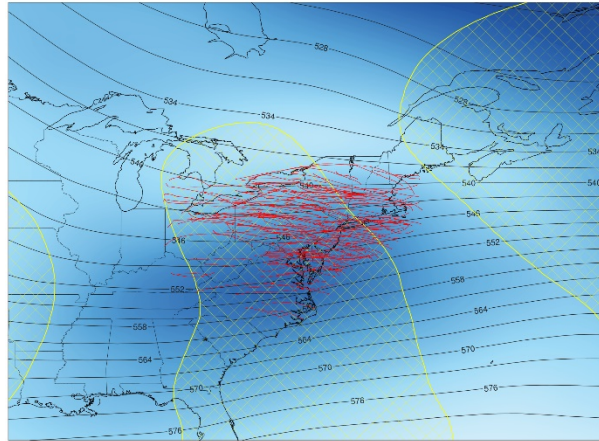with Standard Deviations (m) and <0.01 Significance (hatching)

Figure 23: Average 500 hPa North American Regional Reanalysis (NARR) composite geopotential height (dm, contoured) with standard deviations (m) and <1% significance (hatched) overlain with band centerlines (red) for the binned band angles shown in Figures 21 and 22.

Alternate banding identification by dBZ PDF

One noteworthy signature from observations of heavily banded events is that the typical unimode but skewed distribution of precipitation reflectivity has a second mode (perhaps in the raw distribution but certainly in the anomalous distribution) that exists between 30 and 40dBZ. This dBZ range is far more frequently observed in convective events outside of banding – but when banded precipitation occurs within winter storms, such dBZ echoes may or may not be associated with convective activity.

Figures 24 and 25 demonstrate an example (the February 2014 Northeast heavily banded blizzard) of this multimode distribution for the cumulative maximum reflectivity field throughout the event (Figure 24) and for the snow component only (Figure 25) for the multiple NCEP NAM operational forecast runs for the event. What is quite evident from these series of images is that there was a consistent second mode of forecast reflectivity between 30 and 35dBZ. The snow component only is provided (Figure 25) not only to focus on the more practical impact of winter storms (heavy snow) but also because the restriction removes the just-offshore higher dBZ associated with either banded rainfall or convection that are not relevant here. Even when this restriction is employed, the bimodal distribution remains – and in fact shifts to even higher dBZ thresholds (between 35 and 40dBZ) on many of the NAM runs.

Figure 26 provides the NCAR GridRad pseudo-verification for this event.   The bimodal structure in the observed reflectivity field exists, consistent with the NAM forecasts. It is worth noting here that there is a bit apples to orange comparison, however. The GridRad is hourly, at much higher resolution spatially than the NAM, and also does not distinguish based on precipitation type.   Nonetheless, the bimodal distribution shown in Figure 24 is repeated here.

Forecast quality of banding

Using the example comparisons shown above, we have categorized the performance of the NAM. An example of seven of the dozens of cases is shown in Table 5. A growing database of these events are being described in this manner and the full analysis (including a much deeper meteorological interpretation) will be given in the Nissenbaum dissertation, which is scheduled to be defended in late 2020 or very early 2021. The PDF of this dissertation will be forwarded to the CSTAR Program Manager when it is available for the complete documentation of the research results on this component of the grant.
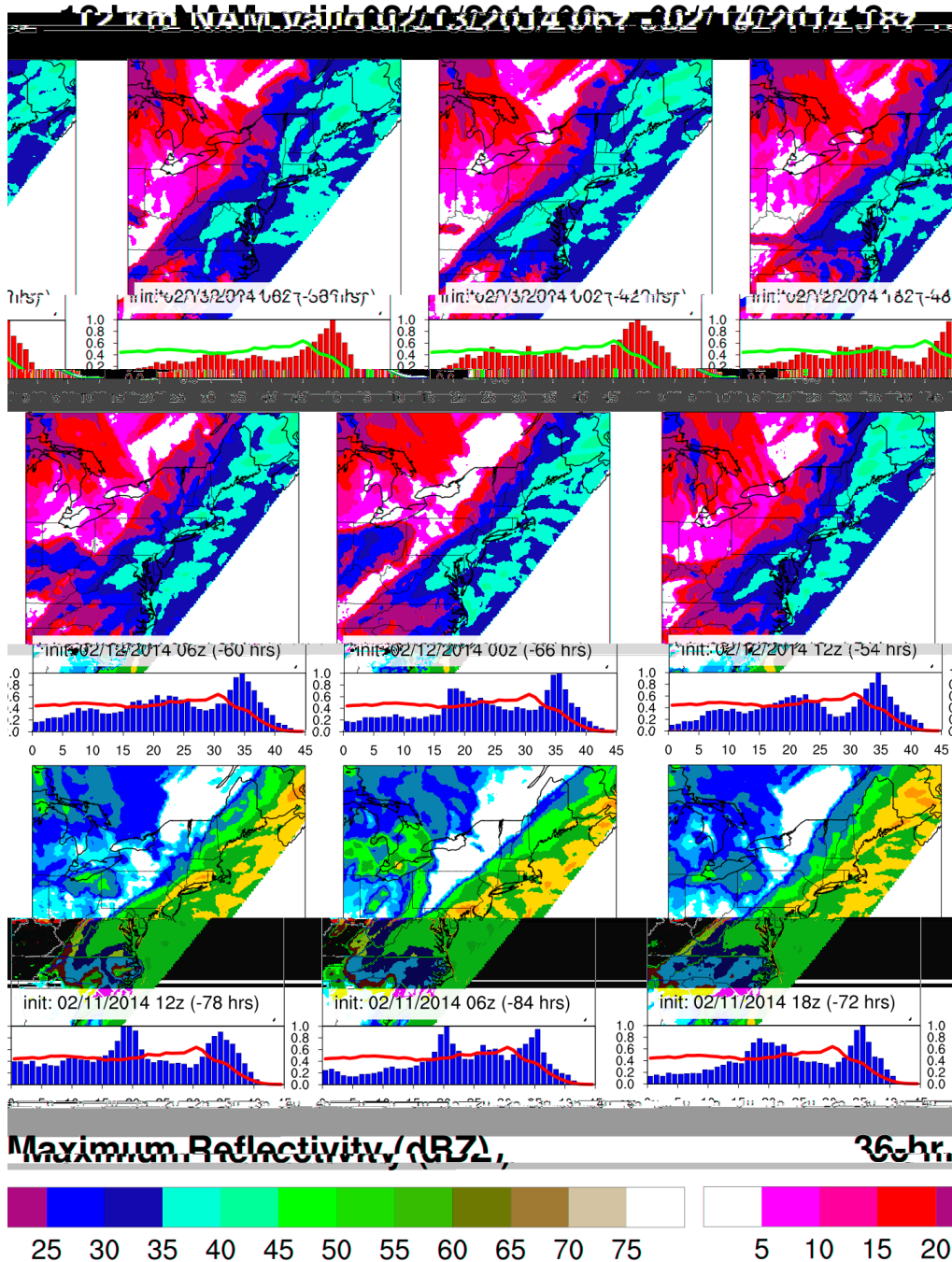
Figure 24: *A second proposed simple but objective measure of banding potential as forecast by numerical models. The maximum forecast reflectivity for each gridpoint over the period of the storm, with associated histograms of binned reflectivity for each run. The example shown here is for a major heavily banded blizzard across the northeast. The histograms shown here very clearly show bimodal (or even trimodal) distribution of reflectivity, with a primary mode often around 35dBZ. The red line represents the climatological mean across all events in the database. Similar analyses exist for all cases in the study and a comprehensive quantification of banding potential using this and other metrics is in the dissertation of Mark Nissenbaum.*
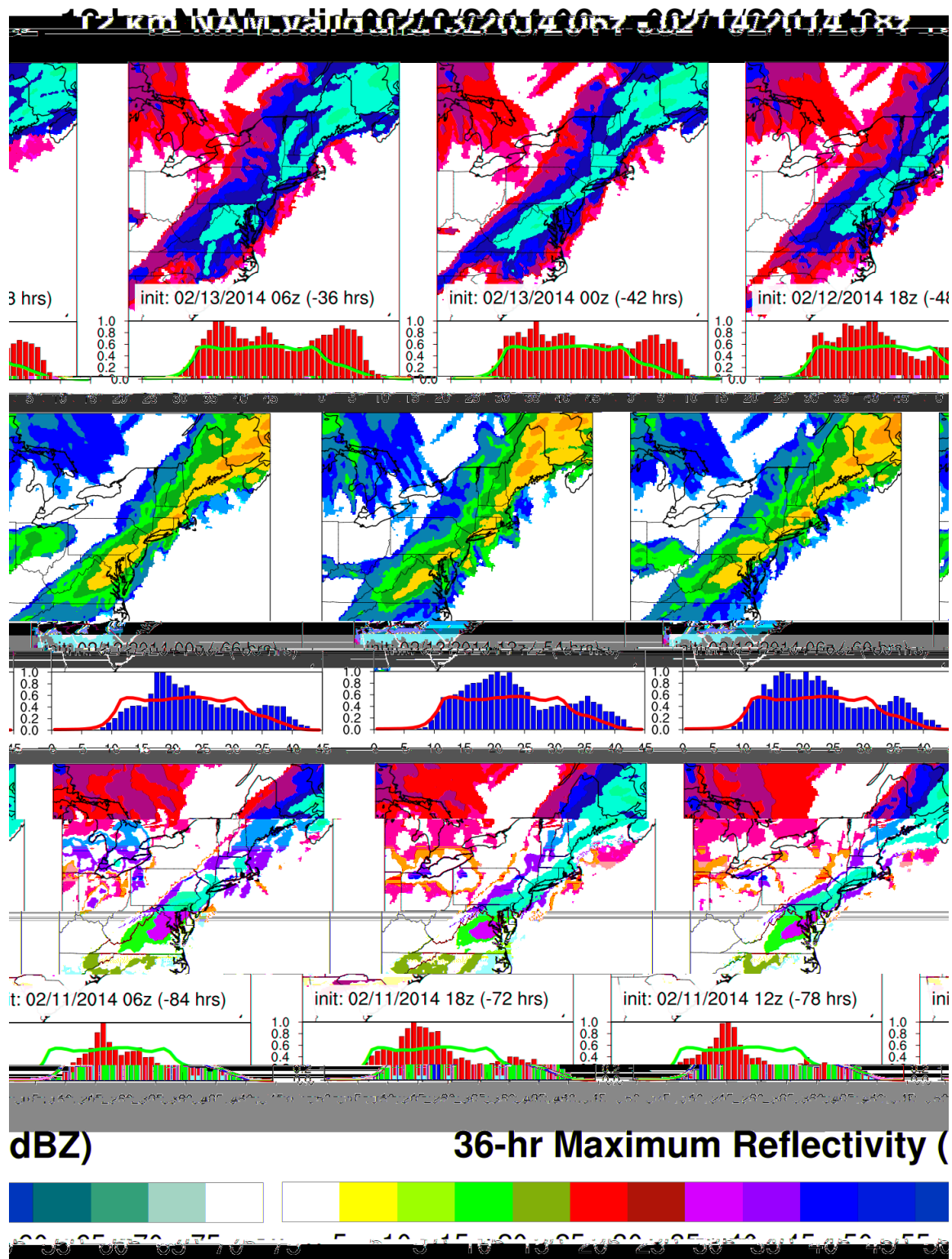
Figure 25: *As in Figure 24, except for snow only according to the model precipitation type algorithm. By focusing on the snow component only, the revised histograms represent more directly the potential for banded precipitation that not only has greater practical impact, but also removes the convection and non-snow banded precipitation offshore.*

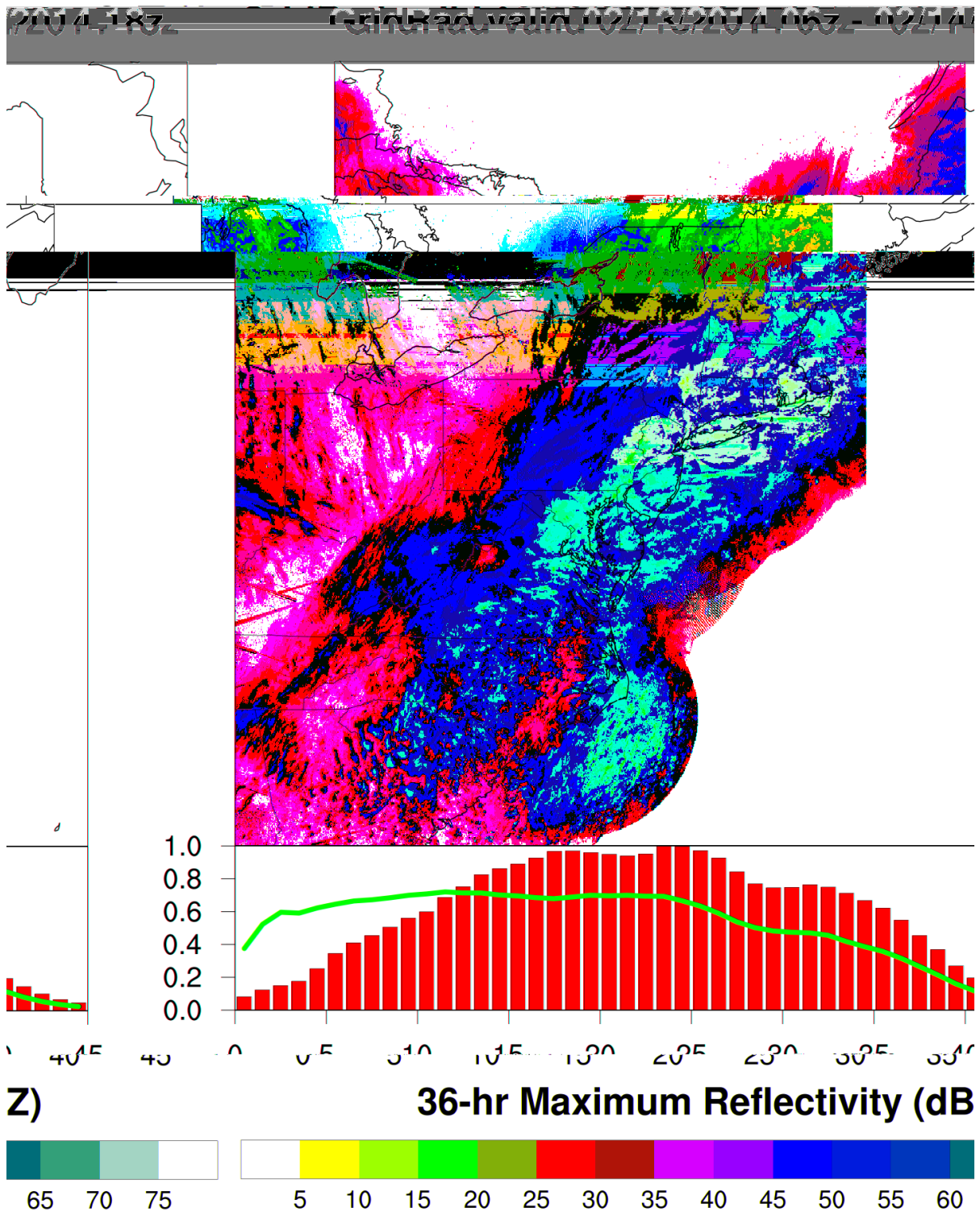**Figure 26**: *As in Figure 24, but using the NCAR GridRad dataset as an approximation to verification for the same case.   The multi-mode distribution forecast by several of the NAM forecasts in Figure 24 and Figure 25 is shown to have verified by the GridRad, with the second mode between 30 and 35dBZ. Note that the cutoff at 70W is due to the limitations of the GridRad dataset and not the algorithm used here.*

Event Date	Comments	NAM Performance Category
28 December 2010	Older model runs suggested heavier precipitation along the coast, but the reflectivity values became weaker in the earlier runs. The placement of precipitation remained similar in all runs. It is likely a single band contributed to much of the high reflectivity values over New England.	2
27 January 2011	Some banding features were present during these model runs. The first indication of banding occurred over Maryland on 78-hour old model run. The signal became stronger on the 54 and 66 hours old runs and reappeared again on the 36-hour old run. The location of the precipitation along the coast was fixed throughout all runs.	2
9 March 2013	This was a weak and localized event. Older model runs placed the bulk of precipitation over New York and Pennsylvania, while earlier model runs placed the precipitation over eastern MA. There is evidence of banding in the 36, 42, and 48-hour old runs.	2
3 January 2014	There were no distinct banding features in any of the model runs. Older model runs (78 and 84 hours ago) were too dry over the mid-Atlantic and too wet over New England. The earliest model run suggest that most of the precipitation fell along the coast.	1
14 February 2014	Banded precipitation was seen over the mid-Atlantic in all model runs. It became less intense over the NYC area in the earlier model runs, while banded precipitation increased over New England. There is even evidence in the earliest model run (36 hours old) of two bands over New England	2
4 February 2015	Banded precipitation was forecast in several of these model runs. The precipitation crept farther north and became heavier in the earlier model runs.	3

Table 5: *A subset of the dozens of cases under examination by the project, with summary comments unique to the case and a currently subjective classification of the NAM forecast performance (1: Poor, 2: Average, 3: Above Average).*

References:

Bosart, L. F., and F. Sanders, 1986: Mesoscale structure in the megalopolitan snowstorm of 11-12 February 1983. Part III: a large-amplitude gravity wave. *J. Atmos. Sci.*, **43**, 924–939, doi:10.1175/1520-0469(1986)043<0924:MSITMS>2.0.CO;2.

Bowman, K. P., and C. R. Homeyer. 2017. GridRad - Three-Dimensional Gridded NEXRAD WSR-88D Radar Data. Research Data Archive at the National Center for Atmospheric Research, Computational and Information Systems Laboratory. https://doi.org/10.5065/D6NK3CR7.

Chen, T. C., M. K. Yau, and D. J. Kirshbaum, 2018: Assessment of conditional symmetric instability from global reanalysis data. *J. Atmos. Sci.*, **75**, 2425–2443, doi:10.1175/JAS-D-17-0221.1.

Corfidi, S. F., M. C. Coniglio, A E. Cohen, and C. M., Mead, 2016: A Proposed Revision to the Definition of "Derecho." BAMS, June 2016, 935-949.

Emanuel, K. A., 1983: On assessing local conditional symmetric instability from atmospheric soundings. *Mon. Weather Rev.*, **111**, 2016–2033, doi:10.1175/1520-0493(1983)111<2016:OALCSI>2.0.CO;2.

Evans, J. S., and C. A. Doswell III, 2001: Examination of Derecho Environments Using Proximity Soundings. Wea. Forecasting, 16, 329-342.

Fantini, M., P. Malguzzi, and A. Buzzi, 2012: Numerical study of slantwise circulations in a strongly sheared prefrontal environment. *Q. J. R. Meteorol. Soc.*, **138**, 585–595, doi:10.1002/qj.947.

Glinton, M. R., S. L. Gray, J. M. Chagnon, and C. J. Morcrette, 2017: Modulation of precipitation by conditional symmetric instability release. *Atmos. Res.*, **185**, 186–201, doi:10.1016/j.atmosres.2016.10.013. http://dx.doi.org/10.1016/j.atmosres.2016.10.013.

Gray, S. L., and A. J. Thorpe, 2001: Parcel theory in three dimensions and the calculations of SCAPE. *Mon. Weather Rev.*, **129**, 1656–1672, doi:10.1175/1520-0493(2001)129<1656:PTITDA<2.0.CO;2.

Hart, R.E., 1997: Forecasting studies using hourly model-generated soundings. M.S. Thesis, Pennsylvania State University, 182pp.

Homeyer, C. R., and K. P. Bowman, 2017: Algorithm Description Document for Version 3.1 of the Three-Dimensional Gridded NEXRAD WSR-88D Radar (GridRad) Dataset. 1–23. GridRad.org.

Klemp, J. B., K. A. Emanuel, and D. J. Raymond, 1984: Dynamics of mesoscale weather systems [presentation]. *NCAR Summer Colloquium 1984*, National Center for Atmospheric Research: Boulder, CO, US.

Kocin, P. J., and L. W. Uccellini, 2004: A Snowfall Impact Scale Derived from Northeast Storm Snowfall Distributions. *Bull. Am. Meteorol. Soc.*, **85**, 177–194, doi:10.1175/BAMS-85-2-177. http://journals.ametsoc.org/doi/10.1175/BAMS-85-2-177.

Lackmann, G., 2012: *Midlatitude synoptic meteorology: Dynamics, analysis, and forecasting*.

Mesinger, F., and Coauthors, 2006: North American Regional Reanalysis. *Bull. Am. Meteorol. Soc.*, **87**, 343–360, doi:10.1175/BAMS-87-3-343. http://journals.ametsoc.org/doi/abs/10.1175/BAMS-87-3-343.

Miller, J. E., 1948: ON THE CONCEPT OF FRONTOGENESIS. *J. Meteorol.*, **5**, 169–171, doi:10.1175/1520-0469(1948)005<0169:OTCOF>2.0.CO;2. http://journals.ametsoc.org/doi/abs/10.1175/1520-0469%281948%29005%3C0169%3AOTCOF%3E2.0.CO%3B2.

Moore, J. T., and T. E. Lambert, 1993: The use of equivalent potential vorticity to diagnose regions of conditional symmetric instability. *Weather Forecast.*, **8**, 301–308, doi:10.1175/1520-0434(1993)008<0301:TUOEPV>2.0.CO;2.

Morcrette, C. J., and K. A. Browning, 2006: Formation and release of symmetric instability following Delta-M adjustment. *Q. J. R. Meteorol. Soc.*, **132**, 1073–1089, doi:10.1256/qj.04.108.

NCEI, 2020a: Global Forecast System (GFS) | National Centers for Environmental Information (NCEI) formerly known as National Climatic Data Center (NCDC). https://www.ncdc.noaa.gov/data-access/model-data/model-datasets/global-forecast-system-gfs.

——, 2020b: North American Mesoscale Forecast System (NAM) | National Centers for Environmental Information (NCEI) formerly known as National Climatic Data Center (NCDC). https://www.ncdc.noaa.gov/data-access/model-data/model-datasets/north-american-mesoscale-forecast-system-nam.

Nicosia, D. J., and R. H. Grumm, 1999: Mesoscale band formation in three major northeastern United States snowstorms. *Weather Forecast.*, **14**, 346–368, doi:10.1175/1520-0434(1999)014<0346:MBFITM>2.0.CO;2.

Novak, D. R., L. F. Bosart, D. Keyser, and J. S. Waldstreicher, 2004: An observational study of cold season-banded precipitation in northeast U.S. cyclones. *Weather Forecast.*, **19**, 993–1010, doi:10.1175/815.1.

Otto, M., and J. Thornton, 2020a: NCEP GFS Home Page. https://www.emc.ncep.noaa.gov/emc/pages/numerical_forecast_systems/gfs.php.

——, and ——, 2020b: NCEP NAM Home Page. https://www.emc.ncep.noaa.gov/emc/pages/numerical_forecast_systems/nam.php.

Schultz, D. M., and P. N. Schumacher, 1999: The use and misuse of conditional symmetric instability. *Mon. Weather Rev.*, **127**, 2709–2732, doi:10.1175/1520-0493(1999)127<2709:TUAMOC>2.0.CO;2.

——, and J. A. Knox, 2007: Banded convection caused by frontogenesis in a conditionally, symmetrically, and inertially unstable environment. *Mon. Weather Rev.*, **135**, 2095–2110,

doi:10.1175/MWR3400.1.

Stein, A.F., Draxler, R.R, Rolph, G.D., Stunder, B.J.B., Cohen, M.D., and Ngan, F., 2015:
NOAA's HYSPLIT atmospheric transport and dispersion modeling system, Bull. Amer. Meteor.
Soc., 96, 2059-2077, http://dx.doi.org/10.1175/BAMS-D-14-00110.1this link opens in a new
window